2

BOLT BERANEK AND NEWMAN INC

CONSULTING · DEVELOPMENT · RESEARCH

CR-103172
Report 1997
Job 11376

RESPONSE OF A RING-STRINGER STIFFENED CYLINDER TO ACOUSTICAL AND MECHANICAL EXCITATION

Get DRA

Terry D. Scharton

Contract No. NAS8-21439

7 April 1971

Submitted to:
National Aeronautics and Space Administration
Marshall Space Flight Center
Huntsville, Alabama 35812

FACILITY FORM 602

N71-25964
(ACCESSION NUMBER)

90
(PAGES)

CR-103172
(NASA CR OR TMX OR AD NUMBER)

(THRU)

63
(CODE)

32
(CATEGORY)

RECEIVED
NASA STI FACILITY
INPUT BRANCH
APR 1971
1 2 3 4 5 6 7 8 9 10 11 12 13 14 15 16 17 18 19 20 21 22 23 24 25 26 27 28 29 30 31

Copy

BOLT BERANEK AND NEWMAN INC
CONSULTING DEVELOPMENT RESEARCH

LOS ANGELES OFFICE
21120 VANOWEN STREET
CANOGA PARK, CALIFORNIA 91303
(213) 347-8360

8 April 1971

George C. Marshall Space Flight Center
National Aeronautics and Space Administration
Marshall Space Flight Center, Alabama 35812

Attn: S & E--ASTN-SVR

Subject: Contract NAS8-21439, BBN Report 1997, "Response of a Ring-Stringer Stiffened Cylinder to Acoustical and Mechanical Excitation"

Gentlemen:

Enclosed are 12 copies and one reproducible copy of the final report, "Response of a Ring-Stringer Stiffened Cylinder to Acoustical and Mechanical Excitation."

Very truly yours,

BOLT BERANEK AND NEWMAN INC.

Terry D. Scharton

TDS:gs
Enclosures
cc: H. C. Thornberry

Do not photograph

CASE FILE

Abstract

The response of a ring-stringer stiffened cylinder to acoustical and mechanical excitation is investigated experimentally and analytically. The results of the investigation confirm the feasibility of using small mechanical shakers attached to the skin of an aerospace vehicle section to simulate the response of the vehicle to acoustic excitation. The results also indicate that the skin vibration, vibration transmission to interior components, and interior sound field resulting from acoustical and mechanical excitations can be predicted adequately using statistical energy analysis techniques at frequencies greater than approximately three times the fundamental resonance frequency.

TABLE OF CONTENTS

LIST OF FIGURES

Figure

Figure

1.0 INTRODUCTION

1.1 Objectives

The primary objective of this study is to investigate the use of mechanical excitation (shakers) to simulate the response of a ring-stringer stiffened cylinder to acoustical excitation. The secondary objective is to develop and experimentally verify analyses for predicting the response of a ring-stringer stiffened cylinder to acoustical and mechanical excitation.

In the environmental checkout of aerospace structures and systems, it is becoming common practice to require full-scale prototype acoustical tests. These tests are justified with the argument that they can uncover effects that may not be seen in simplified analyses or less complete lower level tests. The usual approach in full-scale acoustical testing is to attempt to simulate the excitation, by requiring that the pressure spectrum over some region of the test item is the same as that expected in the service environment. In order to fulfill this requirement, test facilities generating hundreds of kilowatts of acoustical power are being built. Because of the large costs of these highly specialized facilities, it appears worthwhile to examine the possibility of finding a more efficient substitute for full-scale acoustical tests.

For many aerospace structures, we can define an imaginary envelope of external structure that responds directly to the acoustical or aerodynamic environment and subsequently transmits noise and vibration to the internal portions of the system. In these cases we might perform a substitute acoustical test by creating the desired environment on this envelope structure by any convenient excitation. The actual envelope response environment could be estimated by a combination of analytical methods, empirical scaling from existing data, and lower level acoustic tests.

Also, analytical and experimental results show that acoustical and aerodynamic environments with the same pressure spectra do not in general produce the same structural responses.1/ Thus, the use of an acoustical test for inflight simulation can be very misleading if the test spectrum is designed to reproduce the excitation environment. It may be more appropriate to reproduce the response environment.

Above the first few structural resonances, the vibration field generated on the skin of an aerospace vehicle is generally multimodal, consisting of waves incident at many angles, and highly resonant. Thus, the high frequency vibration response can be represented as a reverberant vibration field whose characteristics are analogous to those of a reverberant acoustic field. It is a fundamental property of a reverberant field that the response characteristics are relatively insensitive to the details of the excitation.

1.2 Description of Model

The ring-stringer stiffened cylinder model investigated analytically and experimentally in this study is shown schematically in Fig. 1. The cylinder is 6 ft in length, 3 ft in diameter, and is fabricated from 1/16 in. stainless steel. The cylinder is stiffneed with six T-beam stringers and four T-beam rings as shown in Fig. 1. A sheet metal box has been fabricated and bolted to the interior rings of the cylinder. The box measures 30 in. by 14 in. by 4 in. and is also fabricated from 1/16 in. steel.

In order to investigate the response of the cylinder system to acoustic and mechanical excitation it is convenient to break-up the cylinder system into five subsystems: (1) Exterior Acoustic Field, (2) Cylinder Skin, (3) Rings and Stringers, (4) Box-Mounted to Rings, and (5) Interior Acoustic Field. Figures 2a and b are photographs of the cylinder.

1.3 Summary

Chapter 2 of the report describes analytical predictions and experimental measurements of the response of the cylinder skin and stiffeners to acoustical and mechanical excitation. The results indicate that the cylinder skin response to acoustic excitation can be predicted analytically with reasonable accuracy, particularly at frequencies greater than the ring frequency where the effects of the cylinder curvature are not important. The results of mechanical excitation experiments indicate that small shakers are more efficient at low frequencies when they are attached directly to a cylinder skin and more efficient at high frequencies when they are attached to the stiffening stringers. Results also indicate that the ratio of the stiffener to the skin acceleration is relatively insensitive to whether the cylinder is excited with an exterior acoustic field or with small mechanical shakers attached directly to the cylinder skin.

Chapter 3 describes the response of the box mounted to the stiffeners inside the cylinder. The results indicate that the vibration transfer function from the rings to the interior box is approximately 3 dB higher when the cylinder is excited acoustically than it is when the cylinder is excited with mechanical shakers attached to the stringers. Analytical predictions of the vibration transfer function from the rings to the box agree with the experimental data in the high frequency regime but predict too large a vibration transfer function in the lower frequency regime.

Chapter 4 describes the response of the cylinder interior acoustic field when the cylinder is excited with an exterior acoustic field and when the cylinder is excited with mechanical shakers attached to the stringers. The ratio of the mean-square sound pressure inside the cylinder to the mean-square acceleration of the cylinder skin is virtually independent of whether the cylinder is excited acoustically or with the mechanical shakers for the complete frequency range investigated. Furthermore, analytical predictions of the sound radiated by the resonant motion of the cylinder skin agree well with the measured values of the sound radiated to the cylinder interior over the entire frequency range. Analytical predictions of the cylinder noise reduction, which is defined as the ratio of the mean-square acoustic pressure on the exterior of the cylinder to the mean-square acoustic pressure on the interior of the cylinder, agree well with the measured values in the high frequency regime above 1000 Hz but severely underestimate the measured noise reduction in the low frequency regime.

Chapter 5 describes the design of a conceptual small shaker vibration test to simulate the acoustic response of a typical skin mounted panel on the S IV-B Dry Workshop Forward Skirt. The analysis indicates that one 25-lb rms force shaker exciting the forward skirt skin in the radial direction would result in a panel acceleration response comparable to the response levels specified for the actual acoustic qualification tests of the component.

2.0 RESPONSES OF CYLINDER SKIN AND STIFFENERS

2.1 Response of Skin to Acoustic Excitation

2.1.1 Important Frequencies in the Cylinder Response Calculation

The coincidence frequency is the frequency at which the vibration wavelength in a flat plate is equal to the acoustic wavelength. At frequencies greater than the coincidence frequency f_c, the vibration wavelength is longer than the acoustic wavelength. The coincidence frequency of the cylinder skin is

$$f_c = \frac{\sqrt{3}\, c_o^2}{\pi h_2 c_2} \simeq 8350 \text{ Hz} \quad , \tag{1}$$

where c_o is the acoustic velocity (1100 ft/sec), h_2 is the cylinder skin thickness, and c_2 is the longitudinal wavespeed in the steel cylinder (17,000 ft/sec).

The ring frequency is the frequency above which the curvature of the cylinder may be neglected in considering the vibration characteristics of the cylinder. The ring frequency coincides with the natural frequency of the first breathing mode of the cylinder and is the frequency at which the longitudinal vibration wavelength equals the cylinder circumference. The ring frequency of the cylinder is

$$f_r = \frac{c_2}{2\pi a} = 1800 \text{ Hz} \quad , \tag{2}$$

where a is the cylinder radius.

2.1.2 Mass-Law Acoustic Acceptance

The acoustic acceptance of the cylinder is defined as the space-time mean-square acceleration response $\langle a_2^2 \rangle_{s,t}$ of the cylinder divided by the space-time mean-square pressure $\langle p_1^2 \rangle_{s,t}$ of the exciting acoustic field, where the subscripts on a and p refer to the subsystem definitions in Fig. 1. The response of the cylinder when it is excited by a pressure field in a frequency band Δf is equal to the sum of the responses of the mass-law controlled cylinder modes, which have resonance frequencies less than the exciting frequencies in Δf, and the responses of the resonant cylinder modes, which have resonance frequencies in Δf.

The contribution of the mass-law controlled modes to the acoustic acceptance is easily calculated from $\bar{F} = M\bar{a}$ as[2]

$$\frac{\langle a_2^2 \rangle_{s,t}}{\langle p_1^2 \rangle_{s,t}} \frac{2}{(\rho_2 h_2)^2} , \tag{3}$$

where ρ_2 is the density of steel and the factor of 2 arises from taking account of pressure doubling at the cylinder wall and the random incidence of the acoustic waves.

The mass-law acoustic acceptance may be expressed in decibels as

$$\begin{aligned} AL_2)_{ML} - SPL_1 &= -125 \text{ dB} - 20 \log_{10} W_2 \\ &= -133 , \end{aligned} \tag{4}$$

where $AL_2)_{ML}$ is the mass-law acceleration level in decibels referenced to 1 g, SPL is the sound pressure level in decibels referenced to 0.0002 μbar, and W_2 is the cylinder surface weight in lb_f/ft^2 ($2.4\ lb_f/ft^2$).

2.1.3 Resonance Controlled Acoustic Acceptance

In order to calculate the resonant mode acoustic acceptance, it is convenient to consider three frequency regimes: Regime I where $f > f_c$, Regime II where $f_r < f < f_c$, and Regime III where $f < f_r$.

Frequency Regime I ($f > f_c$)

Following the Statistical Energy Analysis (SEA) approach[3/] (see the Appendix), the resonant response of the cylinder to an external acoustic field is determined from the following power balance relation for the cylinder

$$0 = 2\pi f \eta_2 \, \langle E_2 \rangle_t + 2\pi f \eta_{AF} n_2 [\langle E_2 \rangle / n_2 - \langle E_1 \rangle / n_1] \quad , \qquad (5)$$

where f is the center frequency of the excitation frequency band, η_2 is the internal damping loss factor of the cylinder, $\langle E_2 \rangle_t$ is the time-average total vibrational energy of the cylinder, η_{af} is the acoustically fast (AF) cylinder mode radiation loss factor which governs the cylinder radiation above the coincidence frequency, $\langle E_1 \rangle_t$ is the time-average total energy of the acoustic field, n_2 is the modal density of the cylinder, and n_1 is the modal density of the acoustic space.

In writing Eq. 5, it is assumed that the two ends of the cylinder are sealed and that the power radiated by the cylinder to the acoustic field inside the cylinder is small compared wtih the power dissipated by the internal damping of the cylinder.

The energy of the cylinder is related to the acceleration by

$$\langle E_2 \rangle_t = \frac{\rho_2 A_2 h_2 \langle a_2^2 \rangle_{s,t}}{(2\pi f)^2} \quad , \qquad (6)$$

where A_2 is the cylinder surface area, and the energy of the acoustic field is related to the acoustic pressure by

$$\langle E_1\rangle_t = \frac{V_1}{\rho_o c_o^2} \langle p_1^2\rangle_{s,t} \quad , \qquad (7)$$

where V_1 is the volume of the acoustic field and ρ_o is the density of air. The modal density of the cylinder above the ring frequency is the same as the flat plate modal density n_{fp} given by

$$n_2 = n_{fp} = \frac{\sqrt{3}A_2}{h_2 c_\ell} \quad , \qquad (8)$$

and the acoustic modal density is

$$n_1 = \frac{4\pi f^2 V_1}{c_o^3} \quad . \qquad (9)$$

Combining Eqs. 6-9 with Eq. 5 yields the desired expression for the resonance acoustic acceptance above coincidence

$$\frac{\langle a_2^2\rangle_{s,t}}{\langle p_1^2\rangle_{s,t}} = \frac{2}{(\rho_2 h_2)^2} \frac{\sqrt{3}\pi}{2} \frac{\rho_2 c_o}{\rho_o c_2} \frac{\eta_{AF}}{\eta_{AF} + \eta_2} \quad , \qquad (10)$$

or in terms of decibels

$$AL) = AL)_{ML} + 30 \text{ dB} + 10 \log \frac{\eta_{AF}}{\eta_{AF} + \eta_2} \text{ and}$$

$$AL) - SPL = -103 \text{ dB} + 10 \log \frac{\eta_{AF}}{\eta_{AF} + \eta_2} \quad . \qquad (11)$$

The acoustically fast coupling loss factor η_{AF} is equal to[4/]

$$\eta_{AF} = \frac{\rho_o c_o \sigma_{AF}}{2\pi f \rho_2 h_2} \simeq \frac{5.9}{f} \quad , \qquad (12)$$

where $\sigma_{AF} \simeq 1$ for acoustically fast modes as shown in Fig. 3.[5] The internal loss factor η_2 of the cylinder must be determined empirically. For practical structures, joint damping and other mechanisms often result in an internal loss factor of approximately 10^{-2}.

The effects of the rings and longerons can be ignored in calculating the resonance acoustic acceptance above the coincidence frequency.

Frequency Regime II ($f_r < f < f_c$)

The equations developed in the previous section apply also to this frequency regime except that the acoustically fast mode radiation loss factor η_{AF} and radiation efficiency σ_{AF} must be replaced by the acoustically slow mode radiation loss factor η_{AS} and radiation efficiency σ_{AS}. Thus Eqs. 10-12 become

$$\frac{\langle a_2^2 \rangle_{s,t}}{\langle p_1^2 \rangle_{s,t}} \frac{2}{(\rho_2 h_2)^2} \frac{\sqrt{3}\pi}{2} \frac{\rho_2 c_o}{\rho_o c_2} \frac{\eta_{AS}}{\eta_{AS} + \eta_2} , \qquad (13)$$

and

$$AL_2 - SPL_1 = -103 \text{ dB} + 10 \log \frac{\eta_{AS}}{\eta_{AS} + \eta_2} ; \qquad (14)$$

$$\eta_{AS} = \frac{\rho_o c_o \sigma_{AS}}{2\pi f \rho_2 h_2} = \frac{5.9}{f} \sigma_{AS} . \qquad (15)$$

The acoustically slow radiation efficiency σ_{AS} is calculated from Fig. 3 with

$$\frac{P_2 h_2}{A_2} = 0.01 \qquad (16)$$

where P_2 is twice the length of the six longerons and the two interior rings, plus the length of the two end rings. To account for the fact that the cylinder panel boundary conditions are clamped rather than simply-supported, it is necessary to add 3 dB to the values in Fig. 3. The calculated acoustically slow radiation efficiency is plotted in Fig. 4. Notice that the longerons and interior rings increase thepperimeter in Eq. 16 and thereby increase the acoustically slow radiation efficiency according to Fig. 3.

Frequency Regime III ($f < f_r$)

Below the ring frequency, the curvature of the cylinder is important. The curvature effects the modal density and makes possible AF modes in addition to the AS modes which occur below the coincidence frequency in a flat plate. The AF and AS modes must be treated separately. The modal density of the cylinder below the ring frequency is calculated from Eq. 17.[6]

$$\nu^2 = (1 - u^2)\,\frac{\delta^4}{(\delta^2 + n^2)^2} + \beta^2[\delta^2 + n^2]^2 \quad , \qquad (17)$$

where $\nu = f/f_r = f/1800\ \text{Hz}$,

$\beta = \frac{h_2}{2\sqrt{3}a} = 0.001$, $\delta = \frac{m\pi a}{\ell} = 0.78\ m$, and

$\mu = \text{Poissons ratio} \simeq 1/3$,

where m + 1 is the number of nodes in the axial direction and n is one-half the number of nodes in the circumferential direction. Equation 17 can be rewritten as

$$\nu^2 = \left(\frac{k_a}{k}\right)^4 + \beta^2 a^2 k^4 \quad , \tag{18}$$

where

$$k^2 = k_a^2 + k_c^2 \quad , \quad k_a = \frac{2\pi}{\lambda_a} = \text{axial wavenumber, and}$$

$$k_c = \frac{2\pi}{\lambda_c} = \text{circumferential wavenumber} \quad .$$

Figure 5[7] shows a wavenumber plot of the modes below the ring frequency. Each grid point represents two modes and the grid spacing is $\pi\sqrt{\beta}a/\ell$ in the axial direction and $\sqrt{\beta}$ in the circumferential direction. Shown on Fig. 5 are lines of constant resonance frequency ν.

The solid heavy line divides the wavenumber plot into membrane stress controlled modes governed by the first term in Eqs. 17 and 18 and into bending stress controlled modes governed by the last term in Eqs. 17 and 18.

Acoustically fast modes satisfy the condition that their wavespeed c_{AF} is greater than the speed of sound c_o,

$$c_{AF} \geq c_o \quad . \tag{19}$$

The wavespeed c of a particular mode is given by Eq. 20

$$c = \frac{\omega}{k} = c_\ell \frac{\sqrt{\beta}}{r} (\sin^4 \theta + r^4)^{1/2} \quad , \tag{20}$$

where $r = \sqrt{\beta}ak$ and

$\theta = \sin^{-1} k_a/k$,

and the boundary of AF modes determined from Eqs. 19 and 20 is given by

$$r_{AF}^2 \quad \frac{V_c}{2} - \frac{V_c}{2}\left[1 - \frac{4 \sin^4\theta_{AF}}{v_c^2}\right]^{1/2} \quad , \tag{21}$$

where $V_c = f_c/f_r = 4.6$, is shown in Fig. 5.

The modal densities of AF and AS modes are determined from Fig. 5 or more exactly by manipulation and numerical integration of Eqs. 18 and 21.[8] For simplicity the results are given in Fig. 6.[8] Below the ring frequency f_r, $n_t = n_{AS} + n_{AF} \approx n_{AS}$, since $n_{AF} \ll n_{AS}$. Approximate expressions for n_{AS} and n_{AF} are given by Eqs. 22 and 23 respectively,

$$n_{AS} = \begin{cases} (f/f_r)^{2/3}\,\dfrac{\sqrt{3}A_2}{h_2c_2} & , \quad f < f_r \qquad (22a) \\[2ex] \dfrac{\sqrt{3}A_2}{h_2c_2} & , \quad f_r < f < f_c \qquad (22b) \\[2ex] 0 & , \quad f > f_c \qquad (22c) \end{cases}$$

$$n_{AF} = \begin{cases} (f/f_r)^{2}\,\left(\dfrac{f_r}{f_c}\right)\dfrac{\sqrt{3}A_2}{h_2c_2} & , \quad f < f_r \qquad (23a) \\[2ex] 0 & , \quad f_r < f < f_c \qquad (23b) \\[2ex] \dfrac{\sqrt{3}A_2}{h_2c_2} & , \quad f > f_c\ . \qquad (23c) \end{cases}$$

The effects of the stiffening rings and longerons in this frequency regime have been previously studied.[9] The rings and longerons will have little effect on the modal resonance frequencies and shapes when the spacing between stiffeners is greater than one-half the vibration wavelength of a wave traveling perpendicular to the stiffener. Thus the rings have little effect when

$$d_a > \frac{\lambda_a}{2} = \frac{\pi}{k_a}$$

or

$$k_a > \frac{\pi}{d_a} \quad , \tag{24}$$

where d_a is the ring spacing in the axial direction and the longerons have little effect when

$$d_c > \frac{\lambda_c}{2} = \frac{\pi}{k_c}$$

or

$$k_c > \frac{\pi}{d_c} \quad , \tag{25}$$

where d_c is the longeron spacing in the circumferential direction.

The regions of importance of the rings and longerons are shown in Fig. 5. In addition, it is intuitively plausible that the rings and longerons will have little effect on the resonance frequencies or mode shapes in the entire membrane controlled region since the membrane controlled vibrations do not depend on the cylinder thickness (see first term of Eq. 17). Therefore Fig. 5 indicates that the effect of the stiffeners on the modal vibration characteristics of the cylinder may be limited to the effect of the rings on the AS modes with small axial wavenumbers (Region 2). It should be pointed out that the rings and longerons do, however, increase the radiation efficiency of the AS modes by increasing the radiating perimeter as discussed in the last section.

The resonance acoustic acceptance of the AS and AF modes below the ring frequency can now be calculated as in frequency regime I except that the acoustically fast mode modal density is given by Eq. 23 instead of Eq. 8. The results are

$$\frac{\langle a_{AF}^2\rangle_{s,t}}{\langle p_1^2\rangle_{s,t}} = \frac{2}{(\rho_2 h_2)^2}\,\frac{\sqrt{3}\pi}{2}\,\frac{\rho_2 c_o}{\rho_o c_2}\left(\frac{f}{f_r}\right)^2\left(\frac{f_r}{f_c}\right)\frac{\eta_{AF}}{\eta_{AF}+\eta_2} \qquad (26)$$

and

$$AL)_{AF} - SPL = -110 - 20\log\left(\frac{f_r}{f}\right) + 10\log\frac{\eta_{AF}}{\eta_{AF}+\eta_2} \qquad (27)$$

Similarly, the acoustic response of the AS modes below the ring frequency is given by

$$\frac{\langle a_{AS}^2\rangle_{s,t}}{\langle p_1^2\rangle_{s,t}} = \frac{2}{(\rho_2 h_2)^2}\,\frac{\sqrt{3}\pi}{2}\,\frac{\rho_2 c_o}{\rho_o c_2}\left(\frac{f}{f_r}\right)^{2/3}\frac{\eta_{AS}}{\eta_{AS}+\eta_2} \text{ and} \qquad (28)$$

$$AL)_{AS} - SPL = -103 - 6.67\log\left(\frac{f_r}{f}\right) + 10\log\frac{\eta_{AS}}{\eta_{AS}+\eta_2}\ . \qquad (29)$$

Notice that the radiation loss factor of the AF modes below the ring frequency is the same as the AF modes above coincidence and is given by Eq. 12. Similarly, the radiation loss factor of the AS modes below the ring frequency is the same as the AS modes above the ring frequency and is given by Eq. 15 and Fig. 4.

The total acoustic acceptance below coincidence is equal to the sum of the AF and AS acceptances. The relative importance of the AF and AS cylinder modes below the ring frequency depends on the relative magnitude of η_{AF}, η_{AS}, and η_2 as indicated in Eqs. 27 and 29. In several previous studies of model cylinders,[10,11/] the contributions of the AF and AS modes below the ring frequency were of the same order of magnitude.

2.1.4 Measured Damping Loss Factor of Cylinder

Figure 7 shows measured values of the damping loss factor η_2 for the cylinder. The measurement technique involved exciting radial motion of the cylinder using a shaker driven with an octave band of noise, open-circuiting the shaker coil to remove the excitation force, and measuring the decay rate of the cylinder vibration. A Spencer-Kennedy Decay Rate Meter Model 507 was used to implement this procedure.

The damping values reported in Fig. 7 actually represent the average of two decay-rate measurements on the cylinder skin and two measurements on the longerons. The decay rates measured on the skin and longerons were similar. The dotted and the dashed lines in Fig. 7 represent damping loss factor values measured with the exciting shaker attached to a longeron. The dotted line data corresponds to the case of no external damping applied to the cylinder, and the dashed line data corresponds to the case of eight strips of damping tape applied to each cylinder panel bay. The solid line data in Fig. 7 represents damping values measured with the exciting shaker attached to the cylinder skin and with eight strips of damping tape applied to each cylinder panel bay.

2.1.5 Comparison of Measured and Calculated Cylinder Acoustic Acceptances

Figures 8 and 9 show the calculated and measured values of the cylinder acoustic acceptance, which is the ratio of the cylinder skin acceleration response to the acoustic pressure excitation. Figure 8 corresponds to the case of no external damping applied to the cylinder and Fig. 9 corresponds to the case of eight strips of damping tape applied to each cylinder panel bay.

2.1.5.1 *Measured Results*

The measured results in Figs. 8 and 9, represented by the open dots, were obtained by placing the cylinder in a room excited with a loudspeaker driven with octave-band noise, measuring the octave-band acceleration response at six positions on the cylinder skin, measuring the octave-band sound pressure at many points in the room, and computing the ratio of the octave-band space-time mean-square skin acceleration to the space-time mean-square sound pressure.

2.1.5.2 *Calculated Results*

The theoretical values of the acoustic acceptance shown in Figs. 8 and 9 were calculated using the analytical results in Section 2.1.3 and the values of the cylinder damping loss factor η_2 given by the solid line in Fig. 7.

Region I ($f > f_c$)

The calculated values for the 8000 and 16,000 Hz octave-bands are calculated from Eq. 11 using η_{AF} from Eq. 12.

Region II ($f_r < f < f_c$)

The calculated values for the 4000 Hz octave-band are calculated from Eq. 14 using η_{AS} from Eq. 15.

Region III ($f < f_r$)

Two different calculations are made for this frequency regime. In the first calculation the AS and AF modes are assumed to be uncoupled. The response of the AF modes are calculated from Eq. 27 using η_{AF} from Eq. 12, and the response of the AS modes are calculated from Eq. 29 using η_{AS} from Eq. 15. The responses of the AS and AF modes are summed yielding the prediction represented by the solid line in Figs. 8 and 9.

The second calculation is based on the premise that the rings and longerons tend to couple the AF and AS vibration modes of the cylinder below the ring frequency. Below the ring frequency there are many AS modes, but they are poorly coupled to the sound field. Conversely there are few AF modes, but they are well coupled to the sound field (Figs. 4 and 6). In the second calculation, it is assumed that the AF modes receive the energy from the sound field and then transmit the energy to the AS modes until the modal energy of the AS modes equiparts with the AF modal energy. The resulting cylinder vibration level is calculated by utilizing the AF mode coupling loss factor η_{AF} given by Eq. 12 in Eq. 29 in place of η_{AS} and the result is represented by the dashed line in Figs. 8 and 9.

2.1.5.3 Agreement between Theory and Experiment

The agreement between the theoretical and measured values of the cylinder acoustic acceptance is satisfactory at frequencies above the ring frequency (Regimes I and II) for both the undamped and damped cylinder, Figs. 8 and 9, respectively.

In frequency regime III for the undamped cylinder case (Fig. 8), the measured acoustic acceptance at the ring frequency (approximately the 2000 Hz band) agrees with the second calculation based on coupling between AF and AS modes, whereas the measured value at 250 Hz agrees with the AS mode calculation, and the measured values for the 500 and 1000 Hz bands fall between the AS and coupled mode calculations. These results seem plausible on the basis that the 250 Hz octave-band includes only about one AF mode, Fig. 6, and therefore this mode cannot transfer sufficient energy to all the AS modes to result in the assumed energy equipartition. As one approaches the ring frequency and the number of AF modes increases, the AS modes approach equipartition with the AF modes and the coupled mode model yields good results.

In frequency regime III for the damped cylinder case (Fig. 9), the measured acoustic acceptance agrees well with the first calculation method which assumes that the AS and AF modes are uncoupled. The addition of the damping tape apparently acts to decouple the AS and AF modes. For simplicity, all remaining experiments described herein were conducted with the damped cylinder configurations. (The damped cylinder configuration with a loss factor of approximately $\eta_2 \approx 10^{-2}$ is also more representative of actual built-up aerospace vehicle sections.)

The measured values of the acoustic acceptance in the 125 Hz band lie far below the predicted values in both Figs. 8 and 9. No explanation of this discrepancy between theory and experiment is available. However, it should be noted that the resonance frequency of the first cylinder vibration mode is at approximately 80 Hz and the "Statistical Energy" theory is valid only at frequencies well above the fundamental resonance frequency. In this case, the theory is valid at frequencies greater than approximately three times the fundamental resonance frequency of the cylinder.

2.1.6 Linearity of Cylinder Response to Acoustic Excitation

One objective of this study was to investigate the feasibility of utilizing mechanical shakers to simulate acoustic excitation of a space vehicle or component. In these simulation tests the input to the mechanical shakers would be adjusted so that the space-average vibration level on the vehicle skin or component equals the vibration levels expected with acoustic excitation. Thus in order to utilize mechanical shaker simulation, it is necessary to be able to predict the skin vibration response to an acoustic field on the basis of either (1) semi-empirical prediction techniques, (2) analytical considerations such as those discussed in sections 2.1.2 and 2.1.3, or (3) low-level acoustic test data. The use of low-level acoustic tests to determine the acoustic acceptance would be valid only if the structural response increases linearly as one increases the acoustic pressure. In this section, the results of experiments to determine the linearity of the cylinder response are reported.

Figure 10 shows the undamped cylinder acoustic acceptance measured with three different overall exterior sound pressure levels: 80, 90, and 100 dB. In these experiments, the excitation was broadband noise with a flat one-third octave-band pressure spectrum measured at a point near the cylinder and the response was the one-third octave-band acceleration level measured at one point on the cylinder. At frequencies greater than 250 Hz, the data presented in Fig. 10 indicate that the acoustic acceptance is essentially constant as the sound pressure level is increased, i.e., the cylinder response is linear. Investigation indicates that the apparent nonlinearity reflected in the data of Fig. 10 at frequencies less than 250 Hz is actually caused by a noise floor problem associated with the poor low-frequency response of the low-sensitivity lightweight (2 gms) accelerometer used to measure the cylinder response.

To check the linearity of the cylinder response at low frequencies, a second series of experiments was conducted using an accelerometer with high-sensitivity at the low frequencies and the data from these experiments are shown in Fig. 11. These data indicate that the cylinder response is indeed linear at frequencies down to 50 Hz at the sound pressure levels used in the test (80, 90, and 100 dB overall). Unfortunately, the accelerometer with high-sensitivity at low frequencies weighs 30 gms and results in mass loading of the cylinder at high frequencies.

The frequency above which the accelerometer loads the cylinder is calculated by equating the magnitude of the cylinder skin point impedance to the accelerometer mass impedance. Using the appropriate "infinite-plate impedance" for the cylinder[12/] the mass loading frequency is calculated as

$$\frac{4}{\sqrt{3}} \rho_2 h_2^2 c_2 = 2\pi f_o M_a \quad \text{or} \tag{30}$$

$$f_o \simeq 1250 \text{ Hz} \quad ,$$

where M_a is the heavy accelerometer mass. Above the loading frequency f_o, one expects a 6 dB/octave roll-off in the measured response. Comparison of the data presented in Figs. 10 and 11 confirms the calculated mass loading effect of the heavy accelerometer at frequencies above 1250 Hz. Equation 30 also indicates that the lightweight (2 gm) accelerometers used throughout this research program do not significantly mass-load the cylinder at frequencies below approximately 18,000 Hz.

2.2 Responses of Skin for Mechanical Excitation of the Skin and of the Stiffeners

In this section the relative advantages of attaching the mechanical shakers to the cylinder skin and to the cylinder stiffeners are explored. The advantages explored are of two types. The first advantage concerns the question of which type of attachment results in the maximum cylinder response for a given size shaker. The second advantage concerns which type of attachment results in a more realistic simulation of the response of the cylinder to acoustic excitation.

2.2.1 Maximum Cylinder Skin Response to Mechanical Excitation

The maximum space-time mean-square acceleration response which can be realized on the cylinder skin with two 25-lb force shakers is calculated and measured. The results can be used to determine the number, size, and optimum attachment points of shakers used in a multi-shaker mechanical vibration test of a full-scale aerospace component.

2.2.1.1 Ratio of Cylinder Skin Acceleration to Driving Point Acceleration

The time-average power $<P_{in}>_t$ into the cylindrical structure from a shaker is

$$<P_{in}>_t = \mathrm{Re}[Z_L]<V_o^2>_t \quad , \tag{31}$$

where Z_L is the point force impedance at the driving point of the structure and $<V_o^2>_t$ is the mean-square driving point velocity. The time average power dissipated in the structure $<P_{diss}>_t$ is

$$<P_{diss}>_t = 2\pi f\eta M_s<V_2^2>_{s,t} \quad , \tag{32}$$

where f is the excitation frequency, η is the internal loss factor of the structure, M_s is the structural mass, and $\langle V_2^2 \rangle_{s,t}$ is the space-time mean-square velocity of the cylinder skin panels. Equating the power into the structure to the power dissipated in the structure yields the following expression for the ratio of the skin panel acceleration $\langle A_2^2 \rangle_{s,t}$ to the driving point acceleration

$$\frac{\langle A_2^2 \rangle_{s,t}}{\langle A_o^2 \rangle_t} = \frac{\mathrm{Re}[Z_L]}{2\pi f \eta_2 M_s} \quad . \tag{33}$$

When the shakers are attached to the longitudinal stiffeners, the structural impedance Z_L is assumed to be that of an infinite beam[13]

$$Z_3 = 2\rho_3 (2\pi f \kappa_3 c_3)^{1/2} (1 + i) \quad \text{or} \tag{34}$$

$$= 8.6 f^{1/2} (1 + i) \text{ slugs/sec} \quad ,$$

where ρ_3 is the mass per unit length of the beam, κ_3 is the bending radius of gyration of the beam, and c_3 is the speed of compressional waves of the beam. When the shakers are attached to the skin panels, the relevant structural impedance is the impedance of an infinite plate (see left-hand side of Eq. 30)

$$Z_2 = 16.3 \text{ slugs/sec} \quad . \tag{35}$$

Figure 12 presents the theoretical values of the ratio of the skin acceleration to the driving point acceleration calculated from Eq. 33 for the cases of stiffener and skin excitation. Figure 12 also presents measured values of the acceleration ratio. Two shakers were used in each of the experiments in order to obtain a spatially uniform acceleration response on the cylinder. However, the measured acceleration response was divided by 2 in order to obtain the ratio of skin acceleration to driving point acceleration for a single shaker.

In evaluating Eq. 33 the cylinder mass was interpreted as the total mass of the cylinder skin panels and stiffeners. Figure 12 indicates that for a given driving point acceleration, the power input to the structure is 10-15 dB larger when the shaker is attached to a stiffener than when the shaker is attached to the skin. Thus, if a very large shaker is utilized so that the driving point acceleration is fixed by the shaker stroke or the inertia of the shaker armature rather than by the input impedance of the structure, then maximum power input would be realized by attaching the shaker to the stiffeners.

2.2.1.2 Ratio of Driving Point Acceleration to Free Acceleration of the Shaker

The driving point acceleration depends on the characteristics of both the load and the shaker. The load may be characterized by its impedance Z_L, and the shaker may be characterized by its mean-square free velocity $<V_f^2>_t$ and its driving point mechanical impedance Z_s. The ratio of the driving point acceleration to the shaker free acceleration is

$$\frac{<A_o^2>_t}{<A_f^2>_t} = \frac{|Z_s|^2}{|Z_s + Z_L|^2} \tag{36}$$

The input force impedance of the shaker Z_s should be measured at the shaker head with the shaker coil shorted or, better yet, with the shaker attached to the power amplifier and the input terminals to the power amplifier shorted. For the purpose of calculation, we have represented the input impedance of the Ling V50 MK 1 shakers used in our experiments as simply the calculated inertia of the shaker armature

$$Z_s = i\ 2\ f\ M_s \quad \text{or} \tag{37}$$

$$= i\ 0.04\ f\ \text{slugs/sec} \quad .$$

Equation 37 neglects the effect of the electrical mechanical coupling on the shaker impedance.

The ratio of the driving point acceleration to shaker free acceleration calculated from Eq. 36 is plotted in Fig. 13 for stiffener and skin excitation. The values of the ratio of driving point to free acceleration measured with fixed power amplifier and input levels are also presented in Fig. 13. The measured values of the ratio agree satisfactorily with the theoretical values for the case of skin excitation but do not agree for the case of stiffener excitation. Measurements of the magnitude of the input shaker impedance with the power amplifier input terminals shorted indicate that the impedance varies considerably from the value given in Eq. 37 at frequencies above 2000 Hz. Qualitative considerations indicate that use of the measured shaker impedance values in Eq. 36 would alleviate the large discrepancies between theory and measurements shown in Fig. 13 in the 2000, 4000, 8000, and 16,000 Hz bands.

The power input to the structure from the shaker is related to the shaker and load impedances and the free velocity of the shaker by

$$<P_{IN}>_t = R_e[Z_L] \frac{|Z_s|^2}{|Z_s + Z_L|^2} <V_f^2>_t \quad , \tag{38}$$

or alternatively, to the shaker blocked force, defined as the force generated by the shaker when the armature velocity is blocked

$$<P_{IN}>_t = \frac{R_e[Z_L]}{|Z_s + Z_L|^2} <F_{bk}^2>_t \quad , \tag{39}$$

since

$$\frac{<F_{bk}^2>_t}{<V_f^2>_t} = |Z_s|^2 \quad . \tag{40}$$

Dividing the impedances on the right-hand side of Eq. 39 into the real and imaginary parts and differentiating the time-average power input with respect to the real part of the load impedance and with respect to the imaginary part of the load impedance, it can be shown that the power input is a maximum when the magnitude of the load impedance is equal to the magnitude of the shaker impedance. For a fixed shaker blocked force, the calculated maximum power input occurs at a frequency of approximately 400 Hz for skin excitation and at a frequency of approximately 10,000 Hz for stiffener excitation with the 25 lb force shakers used in these experiments.

2.2.1.3 Maximum Obtainable Levels with Two 25-lb Force Shakers

The Ling V 50 MK 1 shakers used in these experimetns are rated at 25 peak pounds force or 17 rms pounds force. Using Eq. 37 and 40, we calculate a maximum free acceleration of approximately 90 g's rms for these shakers. Fig. 14

shows the measured free shaker acceleration of a Ling V MK 1 shaker driven with the maximum permissible current (approximately 3 amps rms) in octave bands.

Combining the data presented in Fig. 14 with that presented in Figs. 12 and 13 yields in Fig. 15 the maximum expected space-time mean-square skin acceleration levels for octave band excitation with one 25-lb force shaker. Maximum skin acceleration levels range from approximately 3-10 g's rms for the octave bands with center frequencies between 250 and 8000 Hz. The results of sine-sweep experiments indicate that skin panels of the cylindrical structure do not exhibit any vibration modes in the 125 Hz octave band. The absence of modes in the 125 Hz band probably accounts for the low maximum obtainable acceleration response in this frequency band. The Ling V 50 MK 1 shaker exhibits its first structural resonance at approximately 5000 Hz and, therefore, the maximum obtainable acceleration levels roll off at the high frequencies. It is interesting to note that in the low frequency regime, below approximately 1000 Hz, the maximum levels are obtained with the shakers connected to the cylinder skin; whereas in the high-frequency regime, above 2000 Hz, the maximum levels are obtained with the shakers connected to the stiffeners. These results are in qualitative agreement with the fact that the shaker impedance matches the skin panel impedance at approximately 400 Hz and matches the stiffener impedance at approximately 10,000 Hz.

2.2.2 Ratio of Stiffener Acceleration to Cylinder Skin Acceleration

2.2.2.1 Theory for Skin Excitation

The ratio of stiffener acceleration to skin acceleration can be predicted using a two element Statistical Energy

Analysis model (see Appendix). Let element (2) represent the acoustically excited skin and element (3) represent the stiffeners which are excited only via their coupling to the skin. Writing a power balance equation for element (3) yields the following relation for the ratios of the space-time mean-square stiffener acceleration to cylinder skin acceleration

$$\frac{\langle A_3^2 \rangle_{s,t}}{\langle A_2^2 \rangle_{s,t}} = \frac{M_2 N_3}{M_3 N_2} \left(\frac{\eta_{32}}{\eta_{32} + \eta_3} \right) , \tag{41}$$

where M_2 is the total mass of the cylinder skin, M_3 is the total mass of the stiffeners, N_2 is the modal density of the cylinder, N_3 is the modal density of the stiffeners, η_{32} is the coupling loss factor from the stiffeners to the skin, and η_3 is the internal loss factor of the stiffeners.

If we conduct a hypothetical experiment in which we attach a shaker to a stiffener attached to the skin, excite the stiffener, remove the excitation and monitor the stiffener vibration decay, we would intuitively expect the stiffener decay to be dominated by the rate of energy flow from the stiffener to the skin rather than by the rate of energy dissipation in the stiffener. Therefore, we assume that coupling loss factor from the stiffeners to the skin is much greater than the internal dissipation loss factor of the stiffeners ($\eta_{32} >> \eta_3$), and thus Eq. 41 becomes very simple.

The modal density of the skin N_2 is given by Eq. 22a, b, and 23c and the modal density of the stiffeners is given by[14]

$$N_3 = \frac{L_3}{(2\pi f \kappa_3 c_3)^{1/2}} , \tag{42}$$

where L_3 is the total length of stiffeners (rings and longerons), κ_3 is the bending radius of gyration of the stiffeners, and c_3 is the longitudinal wave speed in the stiffeners.

The predicted ratios of cylinder to stiffener acceleration for skin excitation given by Eq. 41 with $\eta_{32} >> \eta_3$ are shown in Fig. 16 as the solid curve.

2.2.2.2 Theory for Stiffener Excitation

The ratio of stiffener acceleration to skin acceleration for the case of stiffener excitation is calculated by writing the Statistical Energy Analysis power balance equation for the unexcited skin system (see Appendix) yielding

$$\frac{\langle A_3^2 \rangle_{s,t}}{\langle A_2^2 \rangle_{s,t}} = \frac{M_2}{M_3} \frac{\left(\eta_2 + \frac{N_3}{N_2} \eta_{32}\right)}{\eta_{32}} \quad . \tag{43}$$

The coupling loss factor η_{32} from stiffeners to the cylinder skin is taken to be the coupling loss factor from a beam to a flat panel given by[15]

$$\eta_{32} = \frac{2\rho_2 h_2{}^{3/2}}{\rho_3} \left[\frac{c_2}{4\pi\sqrt{3}f}\right]^{1/2} \quad . \tag{44}$$

The predicted ratios of cylinder to stiffener acceleration for stiffener excitation given by Eq. 43 with η_{32} calculated from Eq. 44 and with the measured values of η_2 from Fig. 7 are shown in Fig. 16 as a dashed curve.

2.2.2.3 Measured Values of the Ratio of Skin to Stiffener Acceleration

The measured values of the ratio of the space-time mean-square skin acceleration to space-time mean-square stiffener acceleration are also plotted in Fig. 16 for three different types of excitation. The acceleration ratio data obtained with: (1) acoustic excitation are represented by triangels, (2) mechanical excitation of the skin are represented by squares, and (3) mechanical excitation of the stiffeners are represented by circles. Figure 16 indicates that the data for skin and stiffener excitation agree satisfactorily with the respective theories. The data also indicate that attachment of the shakers to the skin more nearly simulates the skin to stringer acceleration ratio in the acoustic excitation case than does the attachment of the shakers to the stiffeners.

3.0 RESPONSE OF BOX MOUNTED TO STIFFENERS INSIDE CYLINDER

This chapter describes a study of the vibration transmission from the rings to the box (Fig. 1) when the cylinder is excited mechanically with three small shakers and acoustically with a reverberant sound field. Calculated values of the vibration transfer function from the ring to the box are compared with measured values in the shaker and acoustic excitation experiments. In the shaker and acoustic excitation experiments, the ends of the cylinder were sealed and the cylinder was lined with acoustic absorption material to reduce the acoustic levels inside the cylinder so that the box vibration levels are governed by the vibration transmitted from the rings to the box.

In addition, the response of the box to only direct acoustic excitation was studied analytically and experimentally. In the latter experiments, the acoustic liner was removed and the box was suspended free of the rings so that the cylinder interior acoustic field was the only source of excitation for the box.

3.1 Vibration Transmission from Rings to Box

In the following, the power input to the box is examined for both a point velocity and a point force source, and the results are used to calculate the vibration transmission from the rings to the box.

3.1.1 Frequency Average Power Input to a Finite Plate from a Point Velocity Source

Let $f_o(f)$ and $v_o(f)$ be the force and velocity at the drive point at frequency f; then the time average power input $<P(f)>_t$ to the finite plate at frequency f is

$$\langle P(f)\rangle_t = \langle f_o(f)v_o(f)\rangle_t \quad , \tag{45}$$

and since the complex force $F_o(f)$ and velocity $V_o(f)$ at the drive point are related to the impedance of the finite plate Z(f) at frequency f by

$$F_o(f) = Z_o(f)V_o(f) \quad , \tag{46}$$

it can be shown that

$$\langle P(f)\rangle_t = R_o(f)\langle v_o^2(f)\rangle_t \quad , \tag{47}$$

where $R_o(f)$ is the real part of the impedance of the finite plate. Now averaging over a frequency band

$$\langle P(f)\rangle_{t,f} = \langle R_o(f)\langle v_o^2(f)\rangle_t\rangle_f \quad . \tag{48}$$

Now for a velocity source the value of $\langle v_o^2(f)\rangle_t$ is independent of the load impedance so (48) reduces to

$$\langle P(f)\rangle_{t,f} = \langle R_o(f)\rangle_f\langle v_o^2(f)\rangle_{t,f} \quad . \tag{49}$$

If we consider an average excitation point on the finite plate, the frequency average resistance $\langle R_o(f)\rangle_f$ of the finite plate is equal to the infinite plate resistance R_∞ of the form of the left-hand side of Eq. 30, so Eq. 49 becomes

$$\langle P(f)\rangle_{t,f} = R_\infty\langle v_o^2(f)\rangle_{t,f} \tag{50}$$

3.1.2 Frequency Average Power Input to a Finite Plate from a Point Force Source

From Eqs. 45 and 46 it can be shown that the time average power input to a finite plate from a point force at frequency f is also given by

$$<P(f)>_t = G_o(f)<f_o^2(f)>_t \quad , \tag{51}$$

where $G_o(f)$ is the real part of the point admittance Z_o^{-1} of the finite plate.

For a force source the value of $<f_o^2(f)>_t$ is independent of the load admittance so that replacing the frequency average value of the finite plate conductance $<G_o>_f$ by the conductance $G_\infty = R_\infty^{-1}$ of an equivalent infinite plate yields for the frequency averaged value of power input

$$<P(f)>_{t,f} = G_\infty<f_o^2(f)>_{t,f} \quad . \tag{52}$$

We now consider the velocity at the force source driving point of the finite plate to consist of a direct field of complex amplitude V_d and a reverberant field of complex amplitude V_r. The direct field is defined as the velocity that would result if the driving force were applied to an infinite plate; and the reverberant field is the difference between the direct field and the actual velocity field on the finite plate. (The reverberant field may be thought of as consisting of the reflections of the direct field waves off the edges of the finite plate.) Thus we have

$$V_o = V_d + V_r \tag{53}$$

where $$V_d \equiv G_\infty F_o \quad . \tag{54}$$

Squaring Eq. 53 and taking the time and frequency average yields

$$\langle v_o^2 \rangle_{f,t} = \langle v_d^2 \rangle_{f,t} + 2\langle v_d v_r \rangle_{f,t} + \langle v_r^2 \rangle_{f,t} \quad . \tag{55}$$

If the frequency band over which we average contains many resonant plate modes the frequency average correlation between the direct and reverberant field is zero so that Eq. 55 becomes

$$\langle v_o^2 \rangle_{f,t} = \langle v_d^2 \rangle_{f,t} + \langle v_r^2 \rangle_{f,t} \quad . \tag{56}$$

Combining Eqs. 9, 10, and 12 yields

$$\langle P(f) \rangle_{t,f} = \frac{1}{G_\infty} \left[\langle v_o^2 \rangle_{t,f} - \langle v_r^2 \rangle_{t,f} \right] \quad . \tag{57}$$

The time-average power dissipated in the finite plate is

$$\langle P_{diss}(f) \rangle_{t,f} = 2\pi f_o \eta m \langle v_r^2 \rangle_{t,f} \quad , \tag{58}$$

where f_o is the center frequency of the frequency band, η is the damping loss factor and m is the plate mass.

It can be shown that the infinite plate conductance G_∞, finite plate modal density N, and finite plate mass are related by[16]

$$G_\infty = \frac{\pi}{2} \frac{N}{m} \quad . \tag{59}$$

Equating the power input (Eq. 50) to the power dissipated (Eq. 58) and using Eq. 59 yields the following expression for the ratio of plate reverberant velocity to driving point velocity

$$\frac{\langle v_r^2 \rangle_{t,f}}{\langle v_o^2 \rangle_{t,f}} = \frac{1}{M + 1} \quad , \tag{60}$$

and the following expression for the power input in terms of the driving point velocity

$$\langle P(f) \rangle_{t,f} = \frac{M}{M + 1} R_\infty \langle v_o^2(f) \rangle_{t,f} \quad , \tag{61}$$

where M is the plate modal overlap index given by $M = \left(\frac{\pi}{2} \eta f\right) N$.

Comparison of Eq. 61 with Eq. 50 indicates that the frequency average power input for a given value of frequency average driving point velocity is lower for a force source than for a velocity source at low frequencies where the modal overlap is less than unity. Similarly comparing Eq. 60 with the corresponding relation for a velocity source

$$\frac{\langle v_r^2 \rangle_{t,f}}{\langle v_o^2 \rangle_{t,f}} = \frac{1}{M} \quad , \tag{62}$$

indicates that the ratio of reverberant velocity to driving point velocity is smaller at low frequencies for a force source than for a velocity source.

3.1.3 Measured Damping Loss Factors of Box

Figure 17 shows measured values of the total damping loss factor η_4 of the box. The loss factor was measured using a decay-rate meter. The measurement involves supporting the box with rubber pads under three attachment bolts and with a small shaker under the fourth bolt. The shaker is excited with an octave band of noise, the excitation is terminated and the decay rate of the box vibration is observed.

3.1.4 Vibration Transmission Calculation and Data

If we assume that the load impedance presented by the box is essentially that of a rigid mass at low frequencies and assign 1/4 of the total box mass to each driving point, the appropriate load impedance is

$$Z_L \approx \text{if slugs/sec} \quad , \tag{63}$$

which is larger than the source impedance presented by the rings, Eq. 34, at frequencies above 144 Hz. Assuming therefore that for $Z_s \quad Z_L$ the force source calculation is applicable, we have from Eq. 60 noting that the acceleration and velocity ratios are equal and including four drive points

$$\frac{\langle A_4^2 \rangle_{s,t}}{\langle A_o^2 \rangle_t} = \frac{4}{M + 1} \quad , \tag{64}$$

which is plotted in Fig. 18 with the box modal overlap M calculated using the measured values of the box damping loss factor shown in Fig. 17.

Also plotted in Fig. 18 are the measured values of the ratio of space-time mean-square box acceleration to time mean-square acceleration of the ring attachment points for both acoustic and mechanical excitation of the cylinder. The vibration ratio is approximately 2-3 dB higher for acoustic excitation than it is for mechanical excitation.

3.2 Direct Acoustic Excitation of Box

For completeness the response of the box to the interior acoustic field was also calculated and measured. If we model the box as a flat plate with the same thickness as the box walls and the same surface area as the box, the ratio of the space-time mean-square acceleration of the box to the space-time mean-square pressure inside the cylinder is given by (see Eqs. 10 or 13)

$$\frac{\langle A_4^2 \rangle_{s,t}}{\langle p_5^2 \rangle_{s,t}} = \frac{2}{(\rho_4 h_4)^2} \, \frac{\sqrt{3}\ \pi \rho_4 c_o}{2\ \rho_o c_4} \, \frac{\eta_{rad}}{(\eta_{rad} + \eta_4)} \quad , \tag{65}$$

where ρ_o is the acoustic density, c_o is the speed of sound, η_{rad} is the box radiation loss factor, and η_4 is the box internal loss factor which has been measured and presented in Fig. 17.

For the 1/16 ft thick steel box, the first factor on the right-hand side of Eq. 65 (the mass law response) is -133 dB. The second term on the right-hand side, which represents the response that must be added to the mass law response to calculate the upper bound resonant response is +30 dB.

Thus Eq. 65 becomes

$$AL_4 - SPL_5 = -103 \text{ dB} + 10 \log \frac{\eta_{rad}}{\eta_{rad} + \eta_4} \tag{66}$$

where the AL_4 is in dB re 1 g and the SPL_5 is in dB re 0.0002 μbar. The radiation loss factor is related to the radiation efficiency σ by

$$\eta_{rad} = \frac{\rho_o c_o}{2\pi f \rho_4 h_4} \sigma = \frac{6}{f} \sigma \quad . \tag{67}$$

The radiation efficiency may be taken from Fig. 3 with $P_4h_4/A_4 = 0.01$ and $f_c = 8000$ Hz. Figure 19 shows a comparison between the measured values of the box acoustic acceptance and the values calculated from Eq. 66. In this experiment, the box was suspended free of the cylinder, the cylinder ends were sealed, and the cylinder was excited with an exterior sound field. The acoustic pressure inside the cylinder was measured at three positions on the axis of the cylinder and the three measurements were averaged. The agreement between calculated and measured values shown in Fig. 19 is satisfactory except in the 125 Hz band.

4.0 RESPONSE OF CYLINDER INTERIOR ACOUSTIC FIELD

4.1 Radiation from Skin to Cylinder Interior

4.1.1 Measurements with Acoustic and Mechanical Excitation

Two experiments were conducted with the ring-stringer stiffened cylinder shown in Figs. 1 and 2. In each experiment the cylinder was positioned on the floor of a reverberant room, and the top of the cylinder was covered wtih 1-in. thick plaster board. The cracks around the top and bottom of the cylinder were filled with clay so that a good acoustic seal was obtained.

In the first experiment, the cylinder was excited with a reverberant sound field generated by placing a speaker in the reverberant room. The experiments were conducted with octave-band noise excitation for the octave bands with center frequencies ranging from 125 Hz to 16,000 Hz. The space-time mean-square acceleration of the cylinder skin was computed from measurements of the mean-square acceleration at a single point on each of six of the cylinder panel bays. Similarly the space-time mean-square acoustic pressure inside the cylinder was computed from measurements of the octave-band mean-square pressure at each of five points. The ratio of the interior acoustic pressure to the skin acceleration computed from these measurements is shown as a function of octave band center frequency in Fig. 20. The sound pressure data is given in terms of dB re 0.0002 μbar and the acceleration data is given in terms of dB re 1 g.

In the second experiment the cylinder was excited with three mechanical shakers attached to alternate stringers. Again the shakers were excited with octave bands of noise.

The space-time mean-square interior acoustic pressure and the space-time mean-square skin acceleration were measured as in the first experiment, and the ratios of the interior sound pressure to the skin acceleration in octave bands are also shown in Fig. 20. The measured ratios of interior sound pressure to skin acceleration are very nearly the same in all octave bands from 125 Hz to 16,000 Hz for both acoustic and shaker excitation.

The experimental data presented in Fig. 20 indicate that the scheme of using mechanical shakers as a substitute for acoustic excitation of an aerospace vehicle is extremely promising, since in the experiment simulation of the skin vibration also resulted in a very close simulation of the interior acoustic environment. One would expect the similarity between the acoustic excitation and the mechanical excitation results to apply equally well to a cylinder with less damping since the vibration response of a lightly damped cylinder is governed by resonant motion of the skin and the resonant motion is insensitive to the means of excitation. If the damping of the cylinder were increased so that the skin vibration were governed by nonresonant skin motion, one might expect some differences in the acoustic and shaker excitation results. However, the damping of the present cylinder (see Fig. 7) is typical of aerospace structures. It would be very difficult to further increase the damping of our experimental cylinder without increasing the skin surface weight, since each panel bay of the cylinder already has eight strips of damping tape.

4.1.2 Theory for Resonant Skin Motion

Theoretical values of the ratio of interior sound pressure to skin acceleration calculated assuming resonant skin motion are also shown in Fig. 20. These values are based upon the following analysis. The time-average power radiated $\langle P_{rad}\rangle_t$ to the cylinder interior by the cylinder skin is given by

$$\langle P_{rad}\rangle_t = R_{rad}\langle v_2^2\rangle_{s,t} \quad , \tag{68}$$

where R_{rad} is the radiation resistance of the cylinder and $\langle v_2^2\rangle_{s,t}$ is the space-time mean-square velocity of the cylinder skin. The time-average power dissipated $\langle P_{diss}\rangle_t$ in the interior acoustic space is given by

$$\langle P_{diss}\rangle_t = 2\pi f_o \eta_5 E_5 \quad , \tag{69}$$

where f_o is the octave band center frequency, η_5 is the total loss factor of the interior acoustic space, and E_5 is the mean-square acoustic energy in the cylinder interior. The radiation resistance is given by

$$R_{rad} = \rho_o c_o A_2 \bar{\sigma} \quad , \tag{70}$$

where ρ_o is the acoustic density, c_o is the speed sound, A_2 is the total cylinder surface area, and $\bar{\sigma}$ is the average modal radiation efficiency given by

$$\bar{\sigma} = \frac{n_{AF}\sigma_{AF} + n_{AS}\sigma_{AS}}{n_{AF} + n_{AS}} \quad , \tag{71}$$

where n_{AF} and n_{AS} are the modal densities of the acoustically fast and slow cylinder modes respectivley, and σ_{AF} and σ_{AS} are the radiation efficiencies of the acoustically fast and slow modes respectivley. The average modal radiation efficiency $\bar{\sigma}$ is calculated from the radiation efficiencies and modal densities given in Figs. 4 and 6 and is plotted in Fig. 21. Note the peaks in the average modal radiation efficiency at the ring frequency and the coincidence frequency. The mean-square acousticaly energy in the interior space is given by

$$E_5 = \frac{V_5}{\rho_o c_o^2} \langle p_5^2 \rangle_{s,t} \quad , \tag{72}$$

where V_5 is the interior volume of the cylinder and $\langle p_5^2 \rangle_{s,t}$ is the space-time mean-square pressure in the cylinder. The total interior loss factor of the acoustic space is given by

$$\eta_5 = \frac{c_o A_2 \alpha}{8\pi f V_5} \quad , \tag{73}$$

where α is the effective absorption coefficient of the cylinder interior which may be related to the reverberation time T_R of the cylinder interior by

$$\alpha = \frac{17.6\pi V_5}{c_o A_2 T_R} \quad . \tag{74}$$

Figure 22 shows values of the cylinder interior acoustic space absorption coefficient α computed from measurements of the interior acoustic space reverberation time T_R in the decay-rate experiments.

Finally, combining Eqs. 68-73 yields the desired expression for the ratio of the cylinder interior pressure to the skin acceleration

$$\frac{\langle p_5^2 \rangle_{s,t}}{\langle a_2^2 \rangle_{s,t}} = \frac{(\rho_o c_o)^2 \bar{\sigma}}{\pi^2 f^2 \alpha} \quad . \tag{75}$$

The theoretical values of the pressure to acceleration ratio computed from Eq. 75 agree well with the measured values of the ratio for acoustic and shaker excitation as shown in Fig. 20.

4.2 Noise Reduction of the Cylinder

In the first experiment, in which the cylinder was excited with a reverberant sound field, the noise reduction of the cylinder was also measured. The space-time mean-square sound pressure in the reverberant room was measured with a microphone mounted on a rotating boom. The noise reduction of the cylinder, defined as the ratio of the space-time mean-square sound pressure in the reverberant room to the sound pressure inside the cylinder expressed in decibels was measured with octave band excitation for center frequencies ranging from 125 Hz to 16,000 Hz and is presented in Fig. 23.

Figure 23 also presents theoretical values of the noise reduction computed according to the following analysis. The ratio of the space-time mean-square pressure in the reverberant room to the space-time mean-square pressure in the cylinder is given by[17]

$$\frac{\langle p_1^2\rangle_{s,t}}{\langle p_5^2\rangle_{s,t}} = \frac{\alpha/\tau}{\left|1 + \dfrac{\sqrt{3}\, c_o^2 \bar{\sigma} B}{8 f h_2 c_2 \eta_2^2}\right|} \tag{76}$$

where τ is the field incidence mass law transmission coefficient, B is a factor which accounts for the effect of curvature on the modal density below the ring frequency, h_2 is the thickness of the cylinder skin, c_2 is the speed of compressional waves in the cylinder skin, and η_2 is the damping loss factor of the cylinder skin. The numerator in Eq. 76 represents the mass law noise reduction of the cylinder, and the second term in the denominator represents the reduction in the mass law noise reduction which results from resonant cylinder mode sound transmission. The mass law field incidence transmission coefficient τ is given by[18]

$$\tau = \left(\frac{2\rho_o c_o}{\pi f \rho_2 h_2}\right)^2 , \qquad (77)$$

The factor B is given by

$$B \equiv \begin{cases} (f/f_r)^{2/3}, & f < f_r \\ 1 & f > f_r \end{cases} , \qquad (78)$$

where f_r is the ring frequency.

Using the measured values of the absorption coefficient α shown in Fig. 22 the computed values of the average radiation efficiency shown in Fig. 21, the calculated values of the mass law field incidence coefficient given by Eq. 77, and the calculated values of B given by Eq. 78; the theoretical value of the noise reduction computed according to Eq. 76 is shown in Fig. 23. The agreement between theoretical and experimental values in Fig. 23 is good at frequencies of 1000 Hz and above. This frequency range extends an octave below the ring frequency and an octave above the coincidence frequency of the cylinder. In the low frequency regime, 125 to 500 Hz, the theoretical calculation severely underestimates the measured noise reduction of the cylinder. An explanation of this is not available at this time, however, the theory represented by Eq. 76 does not take into account the stiffness controlled motion of the interior acoustic space, and this effect can be very important in the low frequency regime.[19]

In the first series of experiments conducted with acoustic excitation of the cylinder the crack at the base and top of the cylinder was not sealed with putty. In these experiments it was noted that the interior sound pressure levels were 10 to 15 dB higher than those predicted. After a good deal of agonizing scrutinization of the data, it was suggested to the author that the sound may be leaking into the interior of the cylinder through the (very small) cracks at the top and bottom of the cylinder, so putty was then applied to seal the cylinder. After the cracks at the top and bottom were sealed, the experimental data with acoustic excitation coincided with the results of the shaker excitation experiments and the theoretical predictions. The moral of this experience is that even a small crack may significantly degrade the noise reduction of a cylindrical structure. The estimated ratio of the open crack area to the total surface area of the cylinder was somewhere in the neighborhood of 1/1000. Therefore, it is possible that the noise reduction of a section of an aerospace vehicle which is vented to the exterior atmosphere may be dominated by acoustic transmission through the vents.

4.3 Comparison of Acoustical and Mechanical Transmission Paths for Box Response

It is interesting to inquire whether the box mounted to the stiffeners inside the cylinder is excited primarily by the mechanical path involving vibration transmission through the box and ring interface or by the acoustic path involving direct acoustic excitation of the box by the interior acoustic field. In a previous study of the vibration response of a spacecraft enclosed in a shroud exposed to acoustic excitation,[20/] it was found that the acoustic transmission path controlled the spacecraft response at low frequencies and the mechanical path controlled at high frequencies.

The box acceleration resulting from only the mechanical path when the cylinder is exposed to an exterior sound field is found by combining the results of Figs. 9, 16, and 18; and the box acceleration resulting from only the acoustic path when the sealed cylinder is exposed to an exterior sound field is found by combining the results of Figs. 23 and 19. Figure 24 shows the ratio of measured box acceleration to exterior acoustic field pressure for the mechanical and acoustical paths. For the stiffener mounted box, the acoustical and mechanical paths are equally important in the low frequency regime, but the mechanical path dominates at high frequencies.

5.0 DESIGN OF A CONCEPTUAL SMALL SHAKER TEST OF A SPACE VEHICLE COMPONENT

In order to investigate the feasibility of utilizing small shakers attached directly to the skin of a space vehicle to simulate the vibration response of space vehicle components to liftoff acoustic and inflight aerodynamic loads, we herein design a conceptual small shaker vibration test of a typical skin-mounted panel (panel #1) on the S-IVB Dry Workshop Forward Skirt.

The panel and mounting configuration are shown in Fig. 25. We calculate the acceleration response at a typical position on the honeycomb panel, when the S-IVB Forward Skirt skin is excited radially with a small shaker delivering 25 lb rms of force with a flat frequency spectrum from 20-2000 Hz (0.3 lb^2/Hz).

In order to perform the calculation we choose the idealized model shown in Fig. 26. The honeycomb panel is assumed to be mounted on a homogeneous flat panel 84 in. on each side. The mass surface density and radius of gyration of the homogeneous panel are calculated from the actual skin (1A) and stringer (1B) configuration. The panel is assumed to have a damping loss factor of $\eta \approx 1/100$ (Q = 100). The honeycomb panel is again modeled as a second homogeneous panel 42 in. in each side and with a surface density and radius of gyration calculated for the actual honeycomb panel. It is assumed that the response point on the honeycomb panel is loaded by a component weighting m = 1 lb.

The procedure is to calculate: (1) the time-average mechanical power $\langle P_1 \rangle_t$ input to plate 1 by the shaker, (2) the time-space average acceleration $\langle a_1^2 \rangle_{s,t}$ of plate 1, (3) the time-space average acceleration $\langle a_2^2 \rangle_{s,t}$ of plate 2, and (4) the time-average acceleration $\langle a_o^2 \rangle_t$ at the mass-loaded point.

5.1 Mechanical Power Input

The mechanical power input is calculated by assuming that plate 1 is infinite. The power input is then

$$\langle P_1 \rangle_t = \langle F^2 \rangle_t G_1 \quad , \tag{79}$$

where $\langle F^2 \rangle_t$ is the mean-square shaker force and G_1 is the infinite plate point conductance given by

$$G_1 = [8 \rho_1 c_1 \kappa_1]^{-1} \quad , \tag{80}$$

where ρ_1 is the surface density of plate 1, c_1 is the speed of longitudinal waves in plate 1 (c_1 = 17,000 ft/sec in aluminum), and κ_1 is the radius of gyration of plate 1.

5.2 Space-Time Average Response of Plate 1

The response of plate 1 is calculated by equating the power into plate 1, Eq. 79, to the power dissipated in plate 1

$$\langle P_1 \rangle_t = \langle P_{diss} \rangle_t = \frac{\eta_1 (\rho_1 A_1) \langle a_1^2 \rangle_{s,t}}{2\pi f} \quad , \tag{81}$$

where η_1 is the damping loss factor of plate 1, A_1 is the area of plate 1, and f is the frequency.

5.3 Space-Time Average Response of Plate 2

The response of plate 2 is calculated by assuming that, since plate 2 is very intimately coupled to plate 1 (for the moment we ignore the rubber isolator strips), the average modal energy θ_2 of plate 2 equates with the average modal energy θ_1 of plate 1

$$\theta_1 = \theta_2 \quad . \tag{82}$$

The modal energy of plate 1 is defined as

$$\theta_1 = \frac{(\rho_1 A_1)\langle a_1^2\rangle_{s,t}}{(2\pi f)^2 N_1} \tag{83}$$

where N_1 is the modal density of plate 1 defined by

$$N_1 = \frac{A_1}{2\kappa_1 c_1} \quad , \tag{84}$$

and the modal energy of plate 2 is defined similarly.

5.4 Time-Average Response of Mass-Loaded Point

The acceleration of the mass-loaded point is calculated from

$$\frac{\langle a_o^2\rangle_t}{\langle a_2^2\rangle_{s,t}} = \left|\frac{R_2}{R_2 + i2\pi fm}\right|^2 \quad , \tag{85}$$

where m is the point mass load and R_2 is the infinite point resistance of plate 2 given by

$$R_2 = 8\rho_2 \, c_2\kappa_2 \quad . \tag{86}$$

Combining Eqs. 79-86 yields an expression for the ratio of the acceleration spectral density of the loaded panel $W_{ao}(f)$ to the force spectral density of the shaker $W_F(f)$

$$\frac{W_{ao}(f)}{W_F(f)} = \frac{\pi f}{4\eta_1\rho_1\rho_2A_1\kappa_2c_\ell} \left|\frac{8\rho_2c_2\kappa_2}{8\rho_2c_2\kappa_2 + i2\pi fm}\right|^2 , \qquad (87)$$

or putting in the numbers from Fig. 26 yields

$$\frac{W_{ao}(f)}{W_F(f)} \quad \frac{4(f/1000)}{|1 + if/1000|^2} [\mathrm{lb}^{-2}g^2] \ . \qquad (88)$$

The attainable acceleration spectral density on panel #1 with $W_F(f) = 0.3$ lb^2/Hz (one 25 lb rms force shaker with a flat spectrum from 20-2000 Hz) is calculated from Eq. 88 and plotted on Fig. 27 which also shows the various qualification vibration test specifications for this type of component.[21/] The calculated attainable acceleration levels are comparable with the test specifications over the frequency range 20-2000 Hz. Note, however, that no isolation between the forward skirt longerons and panel #1 has been assumed in this analysis. The calculated attainable levels should be reduced by an amount equal to the insertion loss of the rubber strip isolators actually used in the mounting of panel #1.

REFERENCES

1. D. A. Bies, "Wind Tunnel Investigation of Panel Response to Boundary Layer Pressure Fluctuations," NASA-CR-501, May 1966.

2. J. E. Manning, R. H. Lyon, and T. D. Scharton, "Transmission of Sound and Vibration to a Shroud Enclosed Spacecraft," BBN Report 1431, submitted October 1966 to NASA Goddard Space Flight Center, Greenbelt, Md., Eq. 98.

3. R. H. Lyon, *Random Noise and Vibration in Space Vehicles*, SVM-1, Shock and Vibration Information Center, United States Department of Defense, 1967, p. 36.

4. Reference 2, Eq. 51.

5. G. Maidanik, "Response of Ribbed Panels to Reverberant Acoustic Fields," *J. Acoust. Soc. Am.* 34 (6), 809, 1962, Eq. 2.24 ($\sigma \equiv R_{rad}/\rho_o c_o A$).

6. Reference 2, Eq. 28.

7. Reference 2, Fig. 8.

8. Reference 2, Fig. 11.

9. K. L. Chandiramani, S. C. Widnall, R. H. Lyon, and P. A. Franken, "Structural Response to Inflight Acoustic and Aerodynamic Environments," BBN Report 1417, submitted July 1966 to NASA Marshall Space Flight Center, Huntsville, Alabama, pp. 42, 52.

10. Reference 2, Fig. 1.

11. T. D. Scharton and T. M. Yang, "Substitute Acoustic Tests," *Shock and Vibration Bulletin* 38, Part 1, p. 118, Eq. 4.

12. Manfred A. Heckl, "Compendium of Impedance Formulas," BBN Report No. 774, submitted to the Office of Naval Research under Contract Nonr 2322(00) Task No. NR 264-017, 26 May 1961, Eq. III-2a.

13. Reference 12, Eq. 2.4.

14. E. E. Ungar and T. D. Scharton, "Analysis of Vibration Distributions in Complex Structures," *Shock and Vibration Bulletin,* 39, Part 5, January 1967, Table 1.

15. Reference 12, p. 47.

16. P. W. Smith, Jr. and R. H. Lyon, "Sound and Structural Vibration," NASA Contractor Report CR-160, March 1965, Eq. IV.7.15.

17. T. D. Scharton, Noise Reduction section of *Procedures for the Analysis of Noise,* submitted to the Litton Industries in support of their proposal on the DX ship, May 1968.

18. L. Beranek, *Noise Reduction,* McGraw-Hill Book Company, New York, 1960, p. 297.

19. R. H. Lyon, "Noise Reduction of Rectangular Enclosures," *J. Acoust. Soc. Am.* 35, 11, Nov. 1963, Fig. 4.

20. J. E. Manning, "A Theoretical and Experimental Model-Study of the Sound-Induced Vibration Transmitted to a Shroud Enclosed Spacecraft," BBN Report No. 1891, submitted 1 May 1970 to Goddard Space Flight Center, Greenbelt, Md., Fig. 34.

21. "Preliminary Vibration, Shock and Acoustic Test Specifications for S-IVB Orbital Workshop (OWS) Components and Subassemblies," George C. Marshall Space Flight Center Memorandum No. S+E-ASTN-ADV-69-153, Dec. 17, 1969.

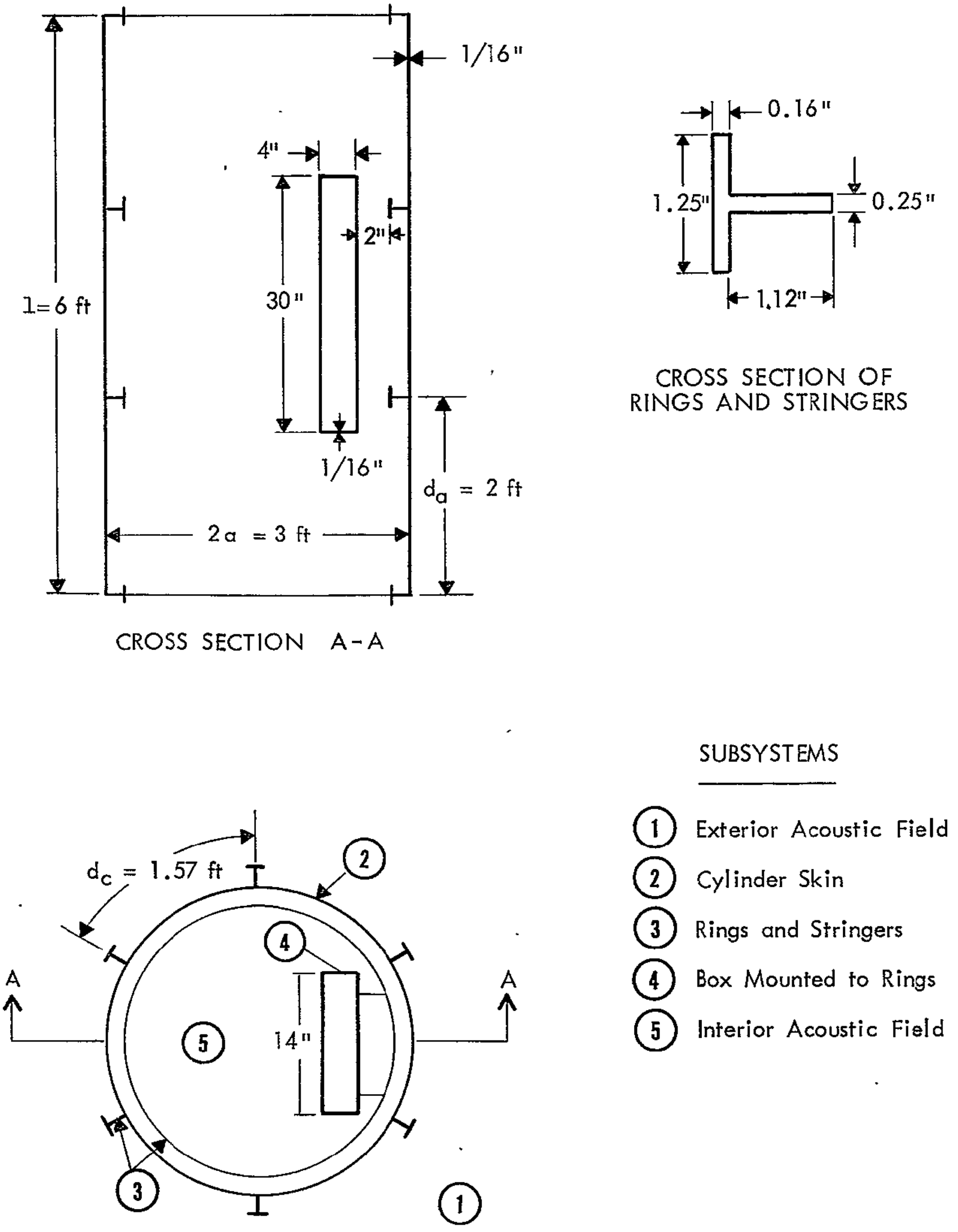

FIGURE 1. RIBBED CYLINDER MODEL

0

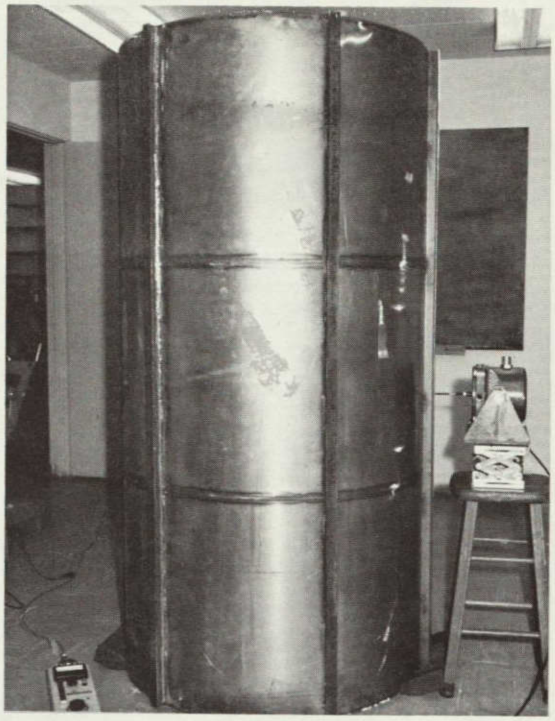

FIGURE 2a. OUTSIDE OF CYLINDER SHOWING LONGERONS

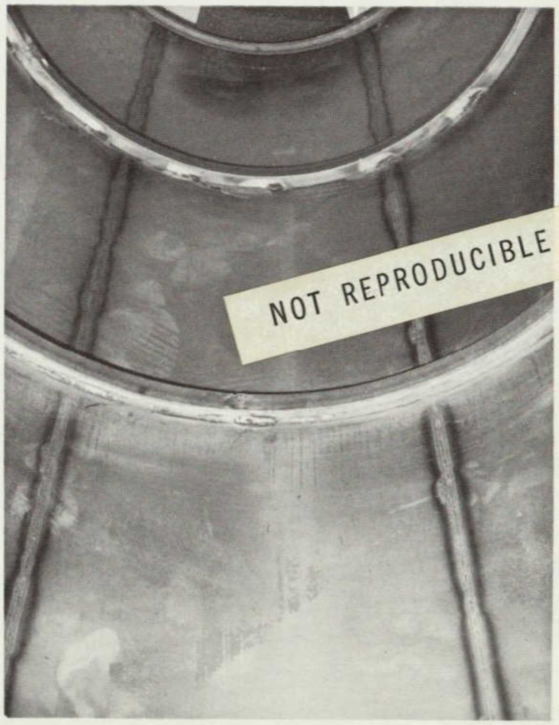

NOT REPRODUCIBLE

FIGURE 2b. INSIDE OF CYLINDER SHOWING RINGS

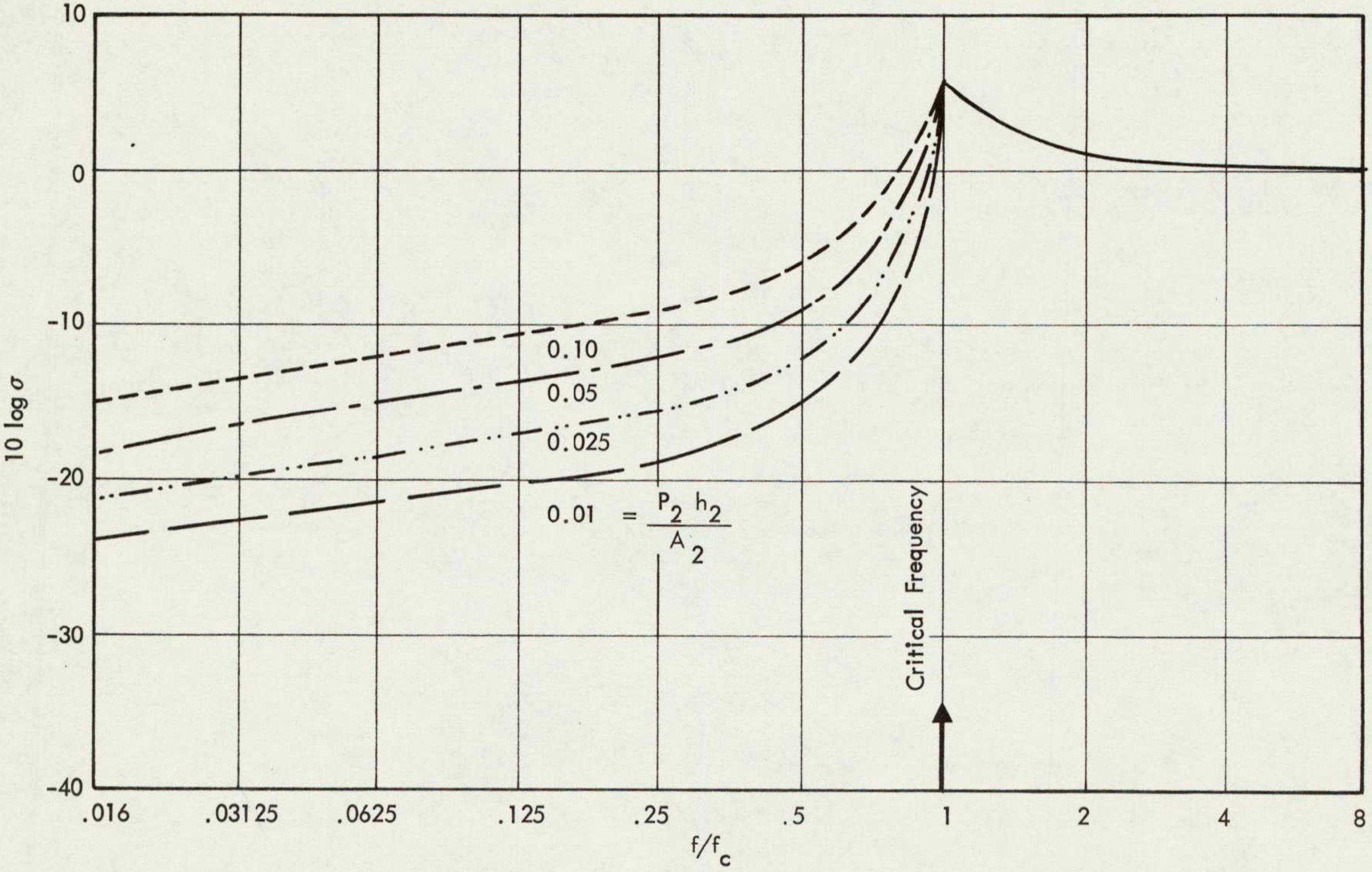

FIGURE 3. RADIATION EFFICIENCY OF STEEL AND ALUMINUM FLAT PANELS (SIMPLE SUPPORTED EDGES)

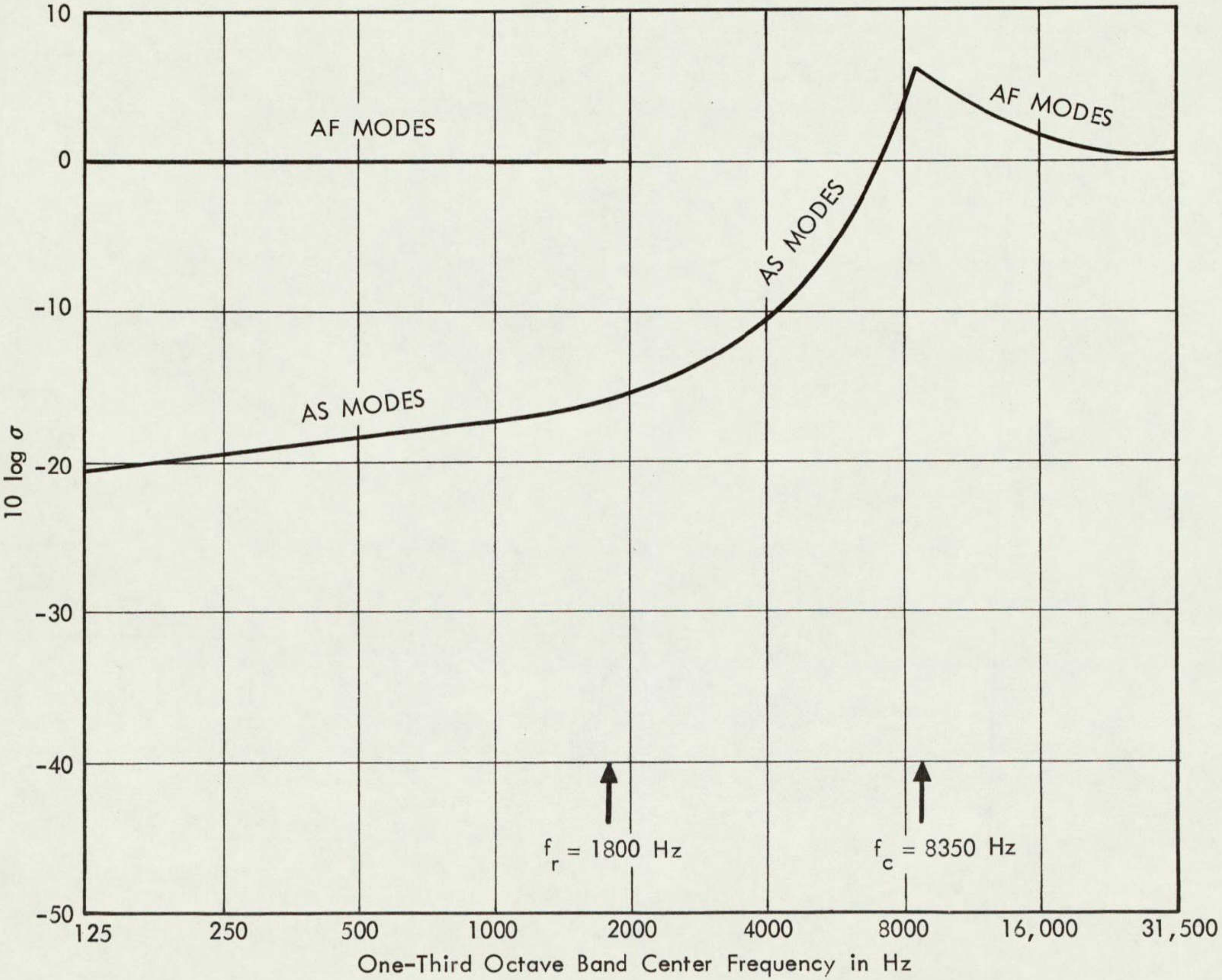

FIGURE 4. RADIATION EFFICIENCY OF CYLINDER

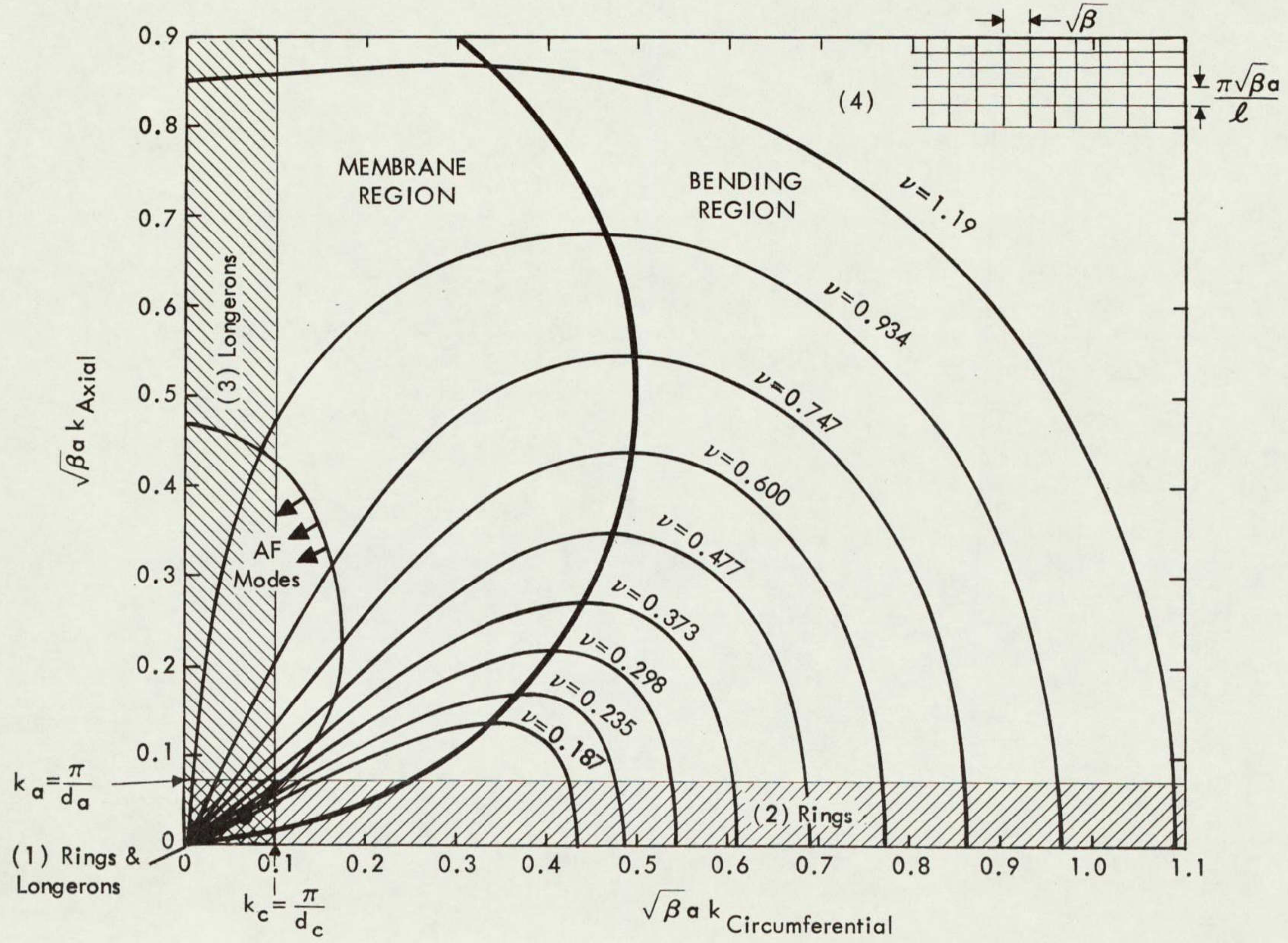

FIGURE 5. WAVENUMBER PLOT OF CYLINDER FOR CALCULATING ACOUSTICALLY FAST AND ACOUSTICALLY SLOW MODES BELOW RING FREQUENCY

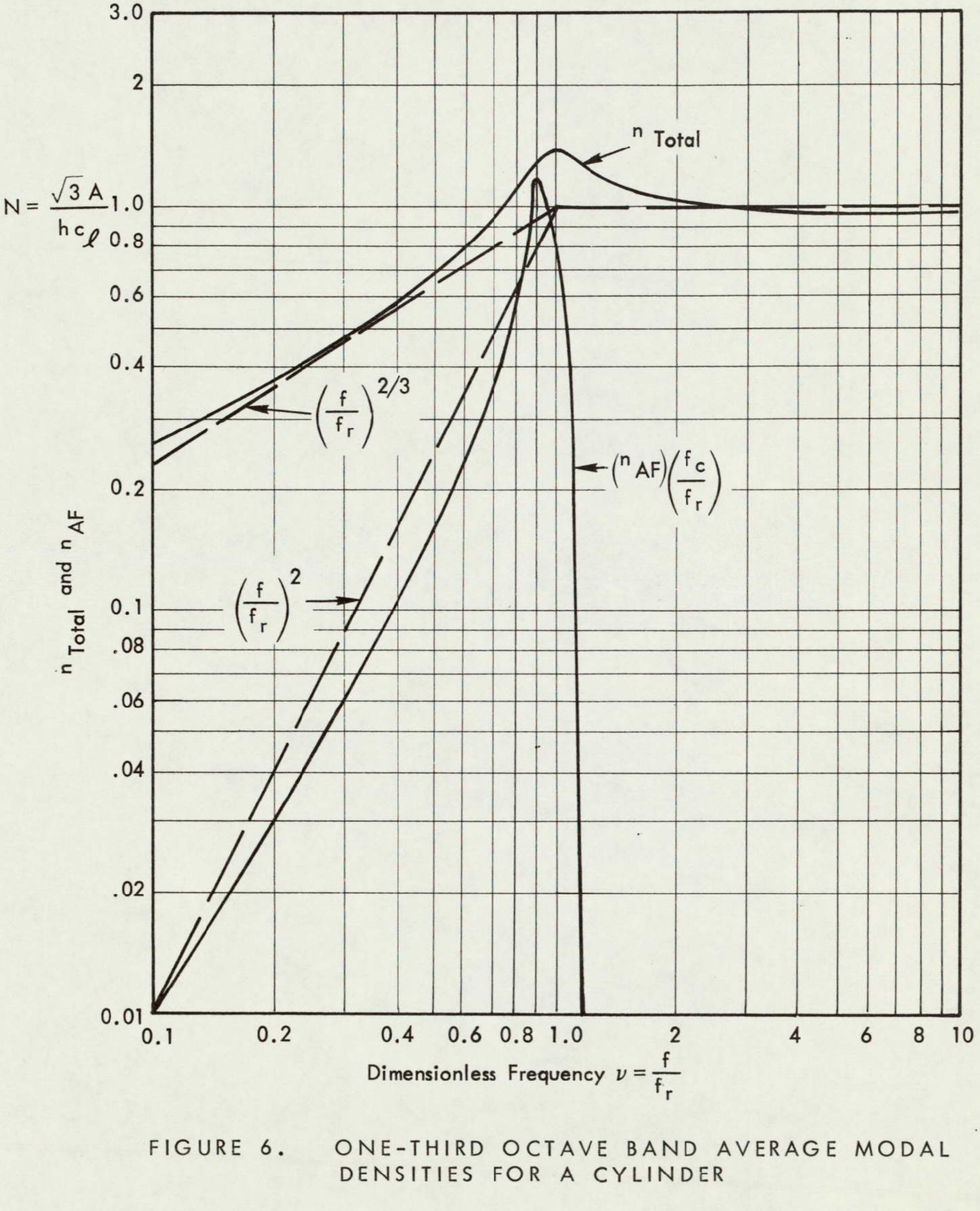

FIGURE 6. ONE-THIRD OCTAVE BAND AVERAGE MODAL DENSITIES FOR A CYLINDER

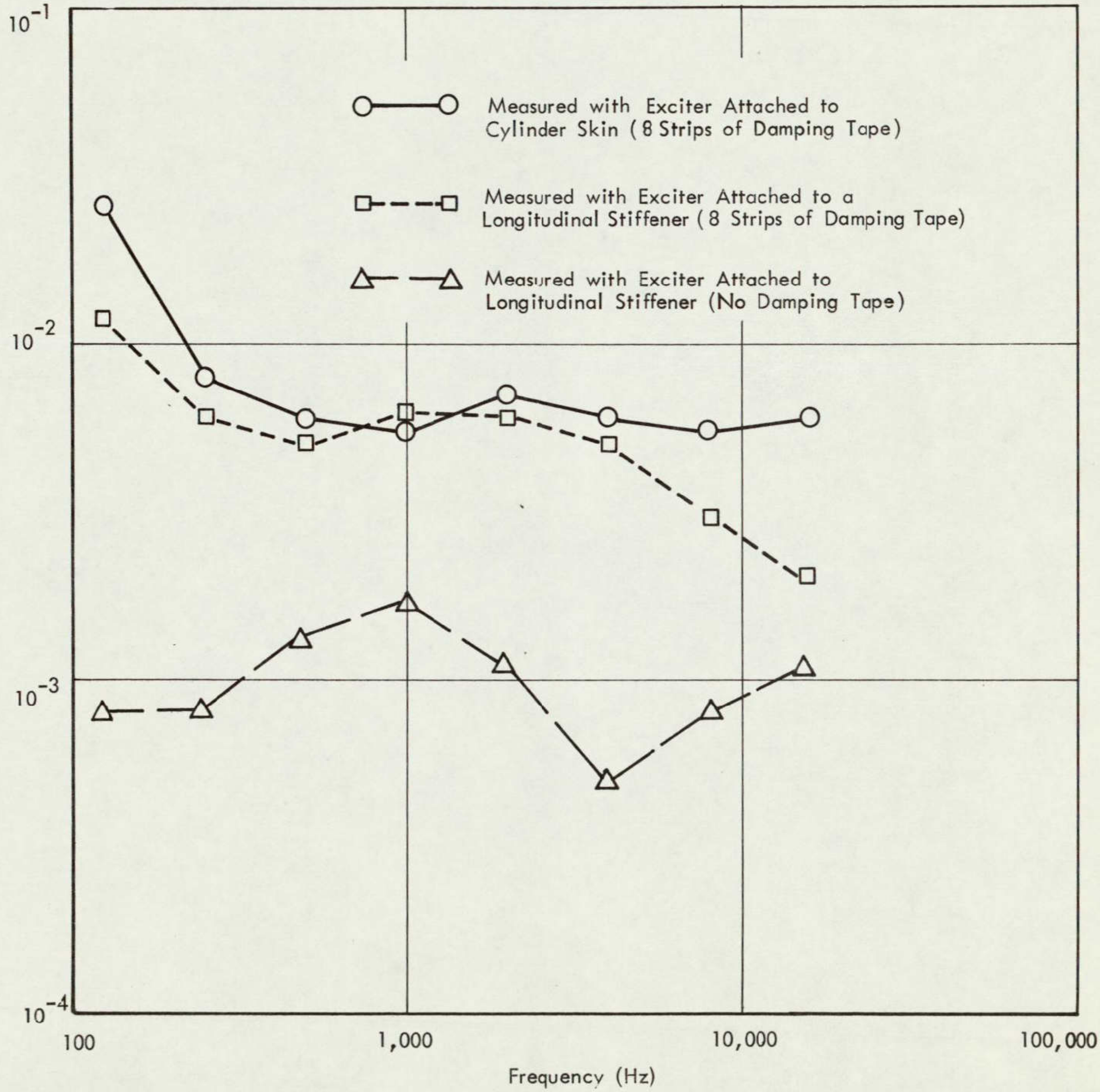

FIGURE 7. MEASURED DAMPING LOSS FACTOR OF CYLINDER

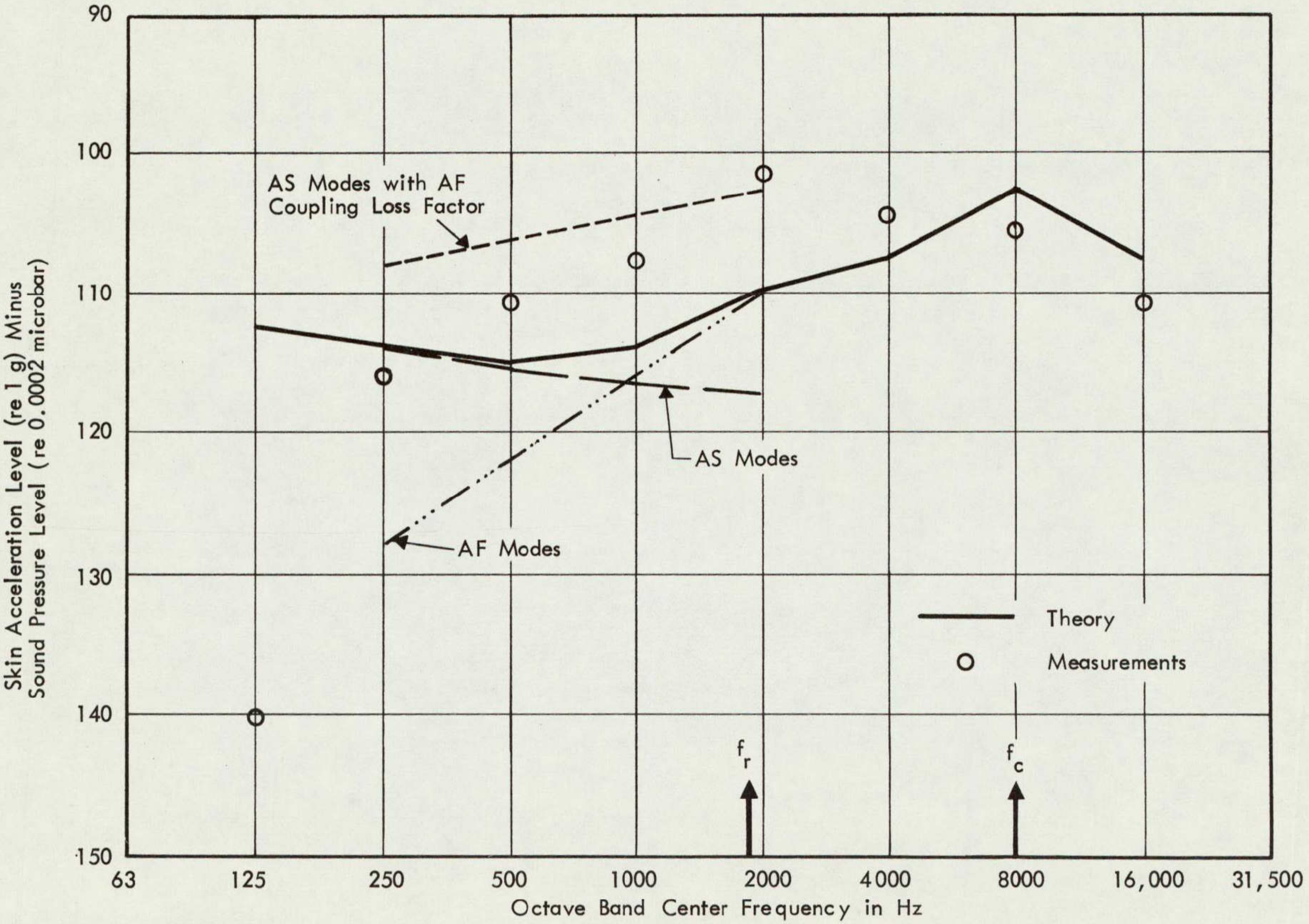

FIGURE 8. THEORETICAL AND MEASURED ACOUSTIC ACCEPTANCE OF UNDAMPED CYLINDER

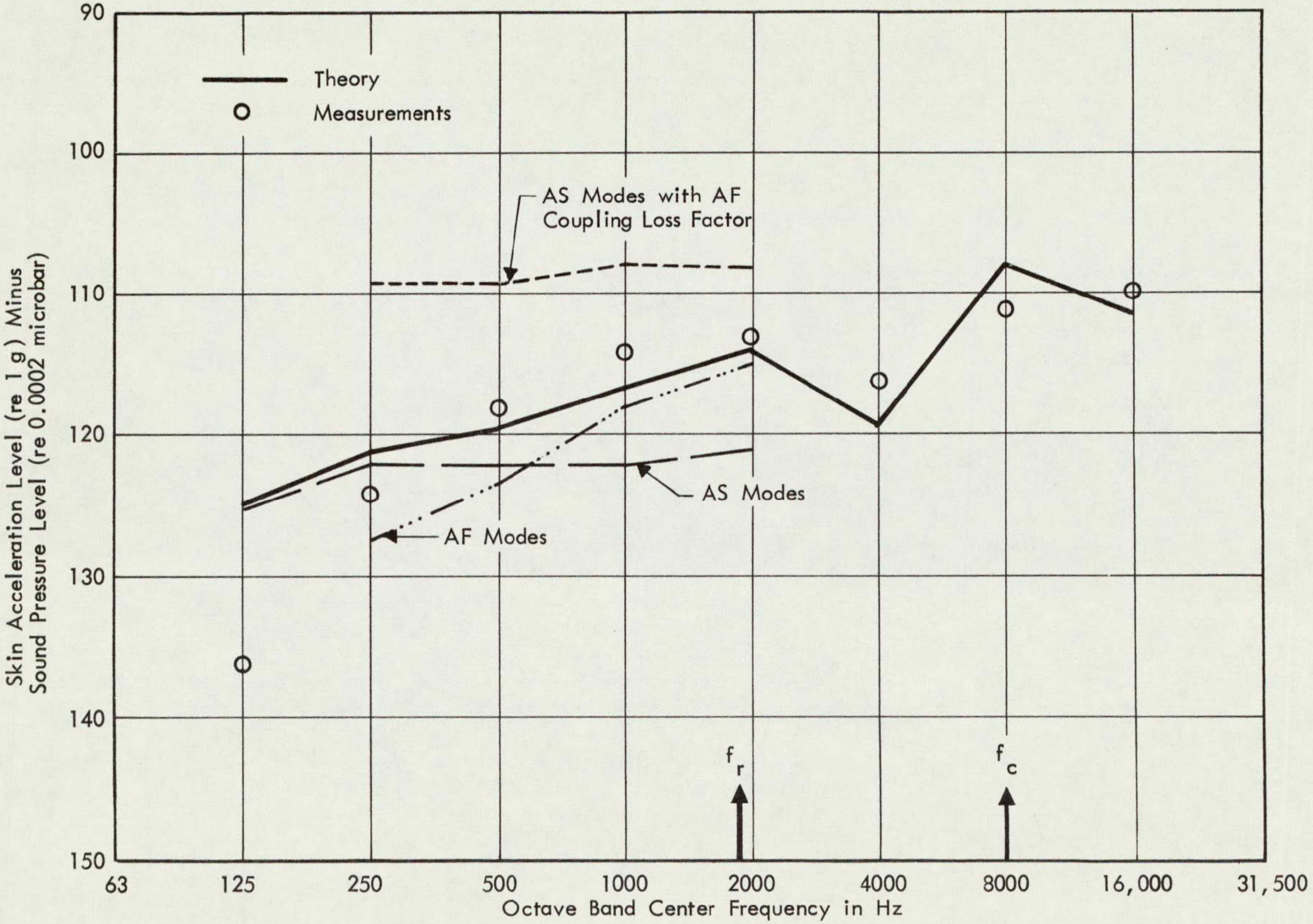

FIGURE 9. THEORETICAL AND MEASURED ACOUSTIC ACCEPTANCE OF DAMPED CYLINDER

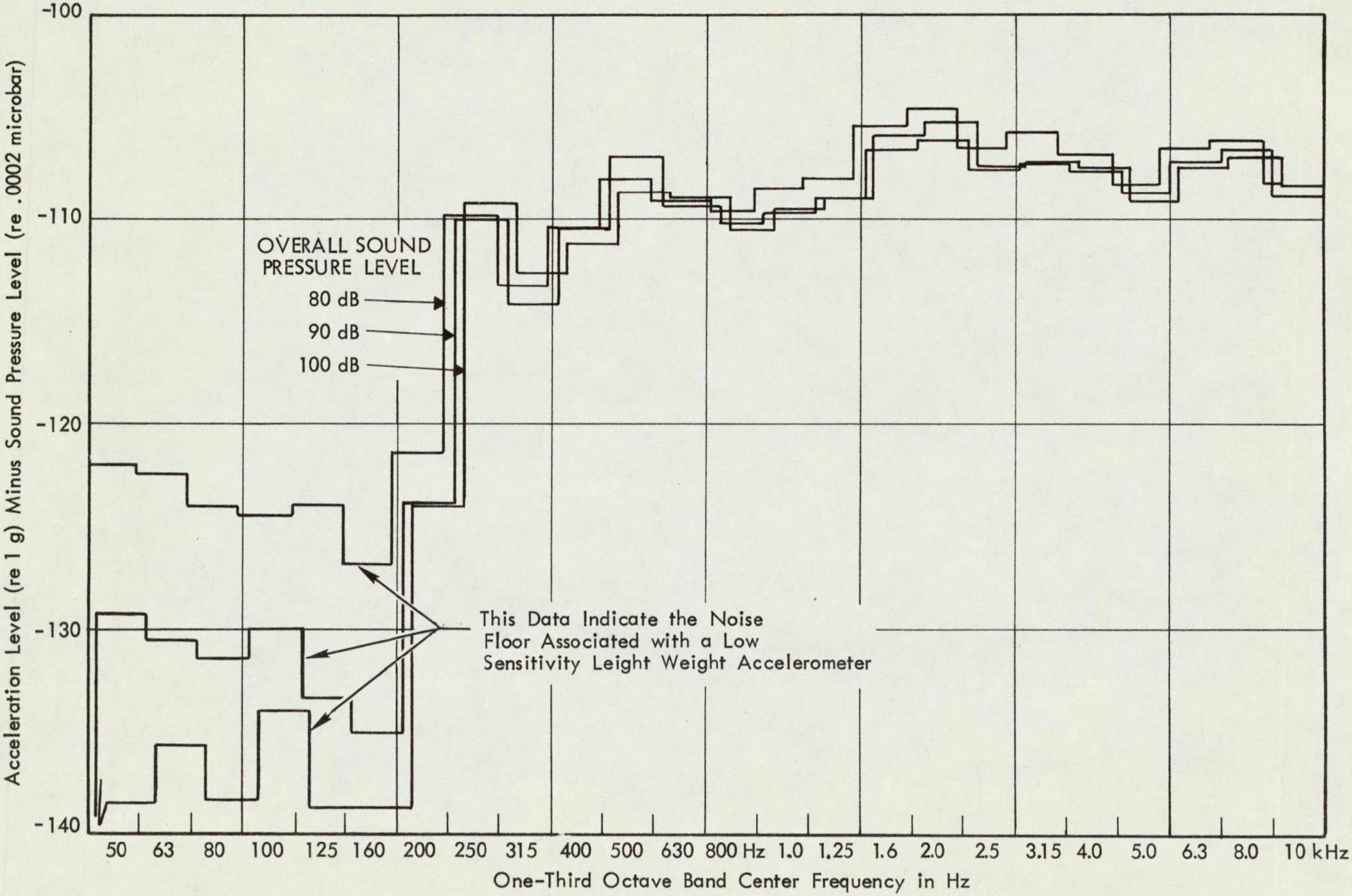

FIGURE 10. ACOUSTIC ACCEPTANCE MEASURED FOR THREE DIFFERENT EXCITATION LEVELS AND WITH LOW SENSITIVITY ACCELEROMETER

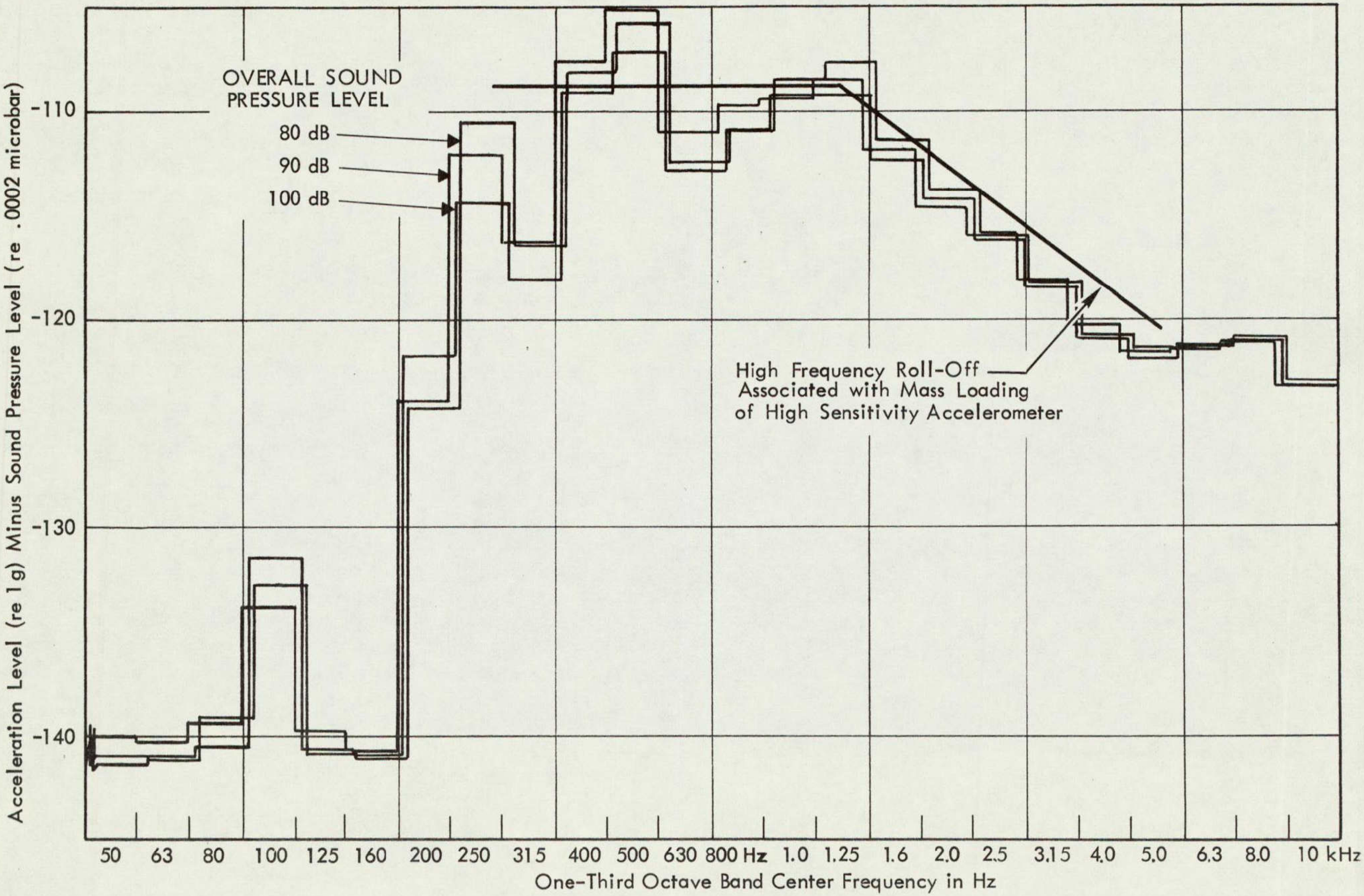

FIGURE 11. ACOUSTIC ACCEPTANCE MEASURED FOR THREE DIFFERENT EXCITATION LEVELS AND WITH HIGH SENSITIVITY ACCELEROMETER

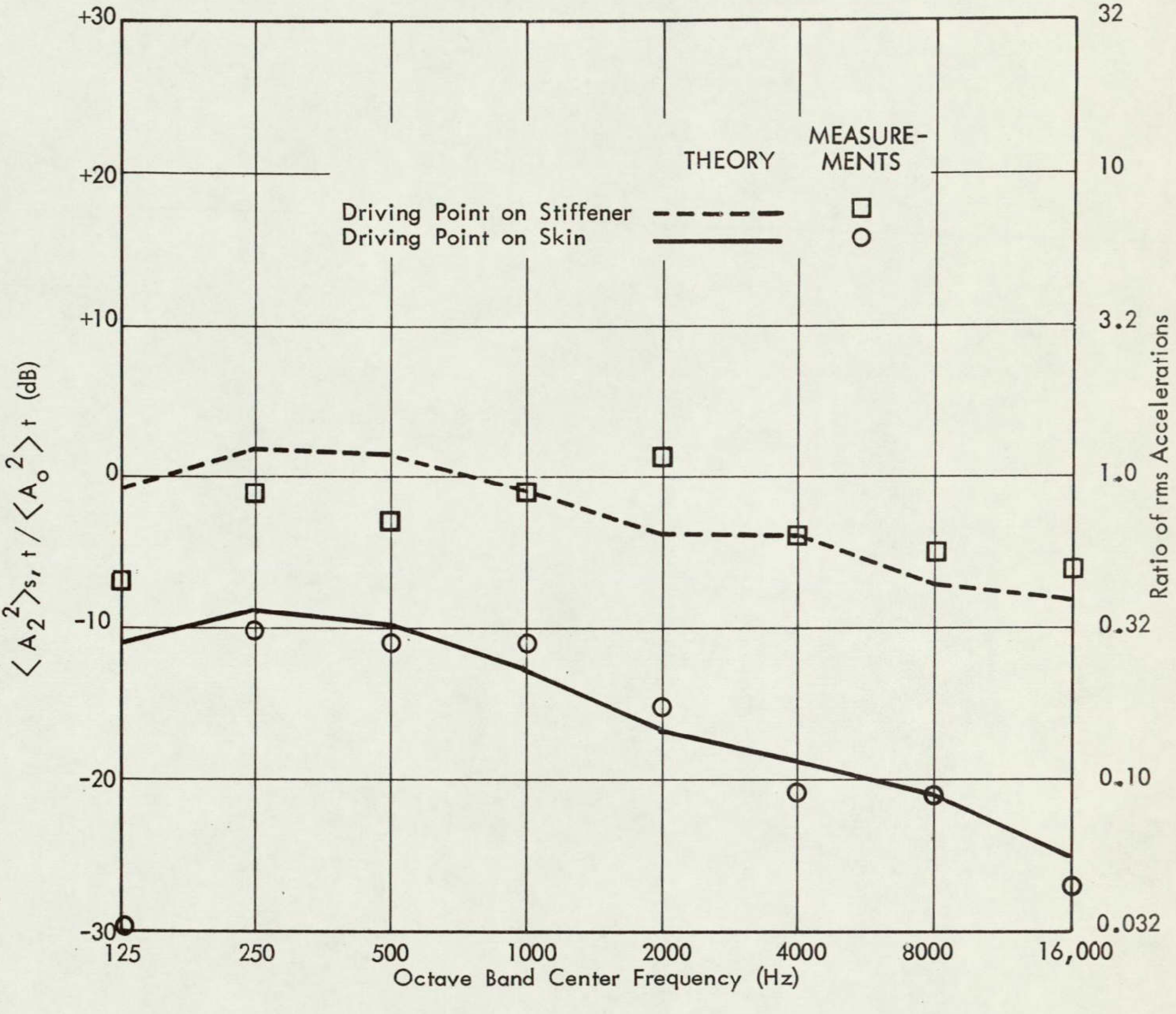

FIGURE 12. RATIOS OF SPACE-TIME MEAN-SQUARE SKIN ACCELERATION TO DRIVING POINT ACCELERATION FOR STIFFENER AND FOR SKIN MECHANICAL EXCITATION

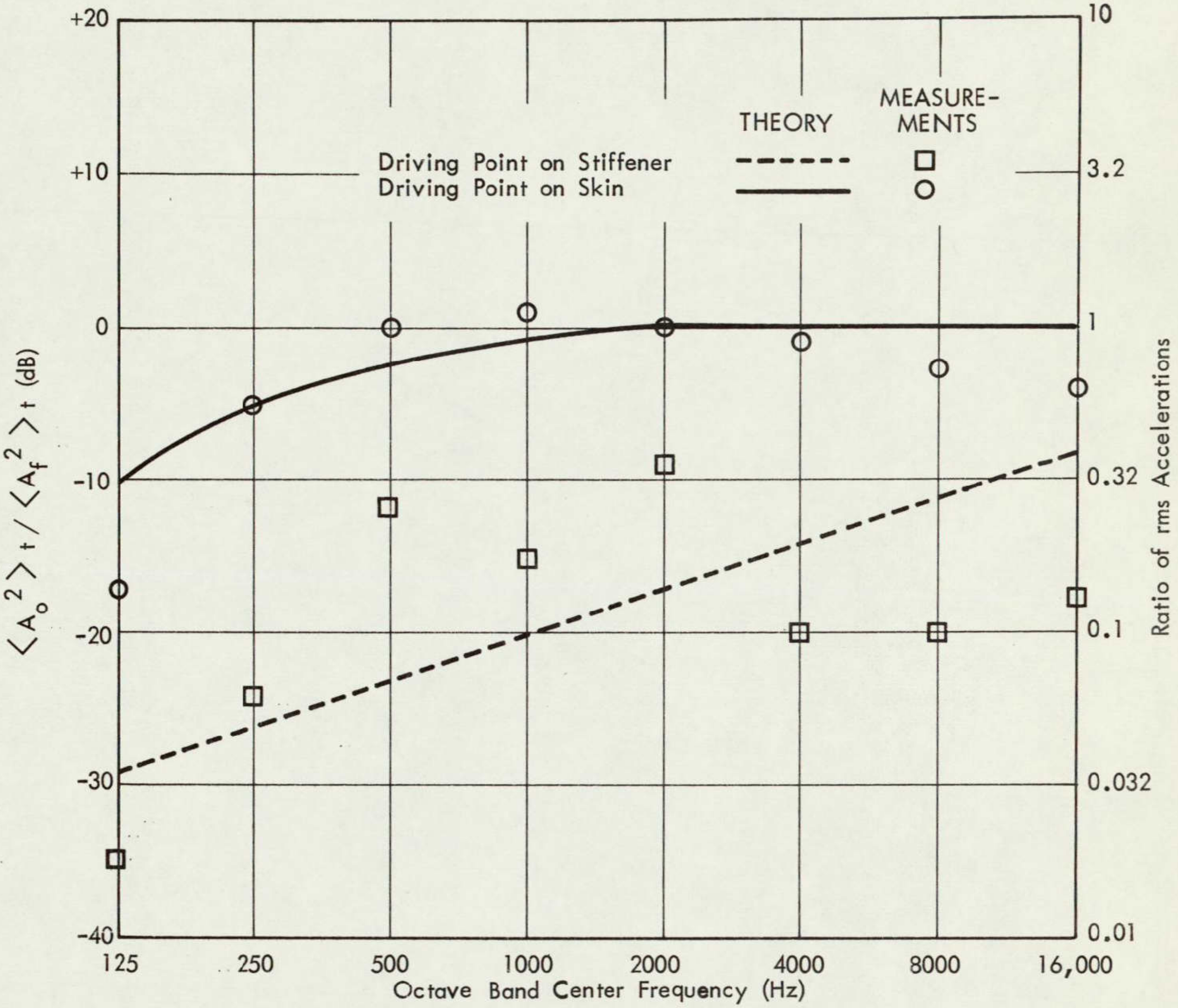

FIGURE 13. RATIO OF DRIVING POINT ACCELERATION TO SHAKER FREE ACCELERATION

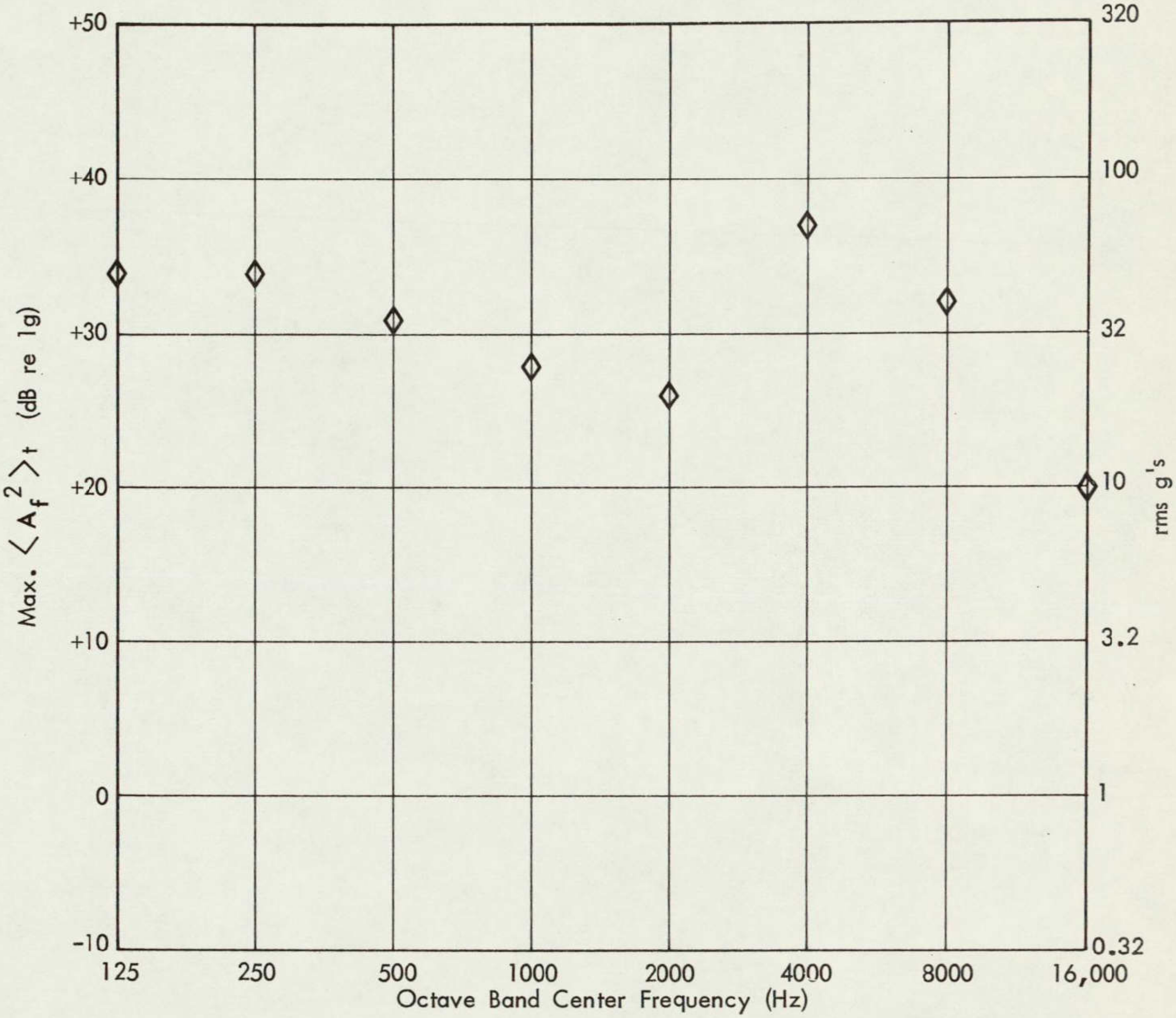

FIGURE 14. MAXIMUM FREE ACCELERATION OF LING V 50 MK 1 SHAKERS FOR OCTAVE BAND EXCITATION

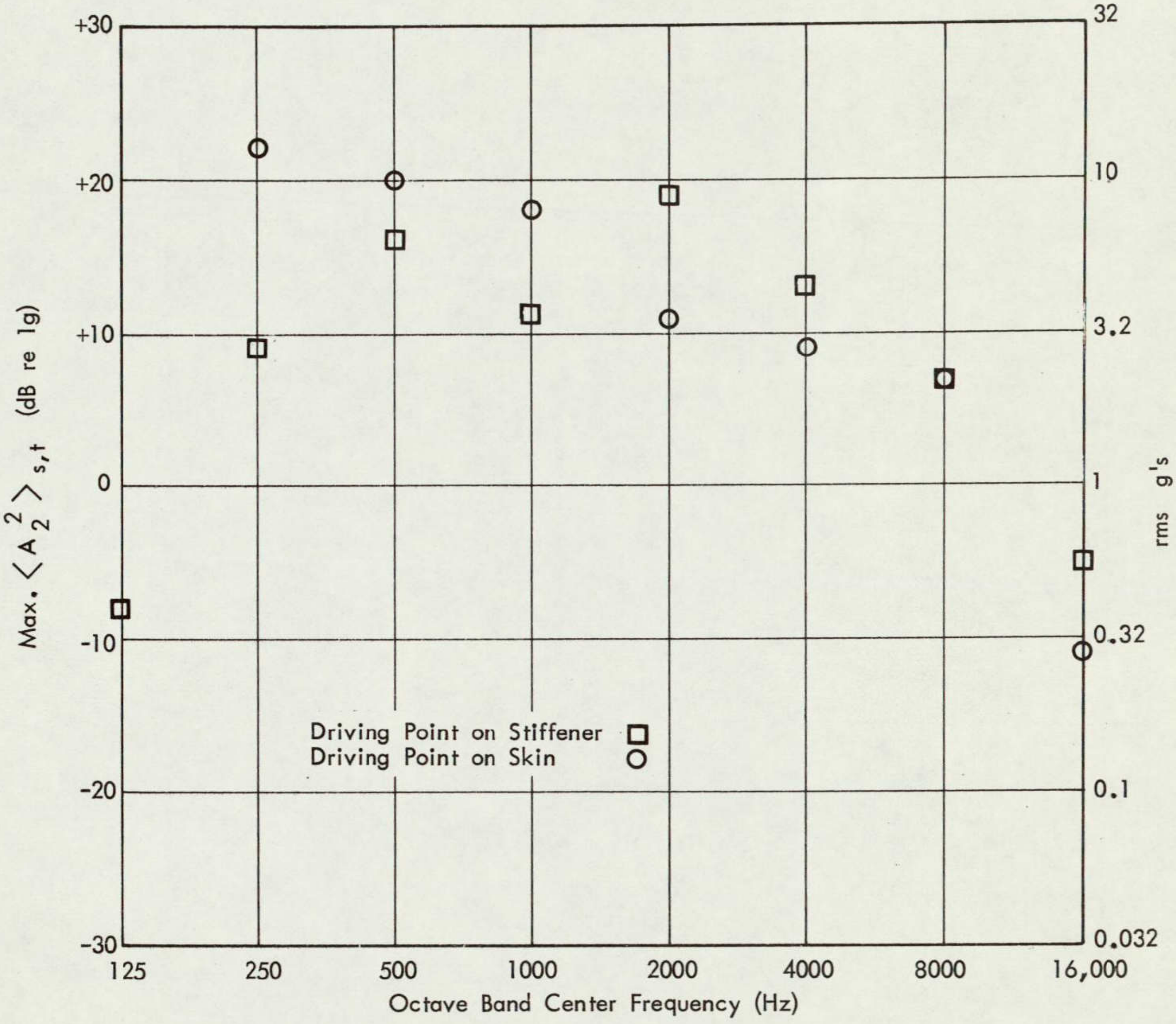

FIGURE 15. MAXIMUM SPACE-TIME MEAN-SQUARE SKIN ACCELERATION FOR OCTAVE BAND EXCITATION

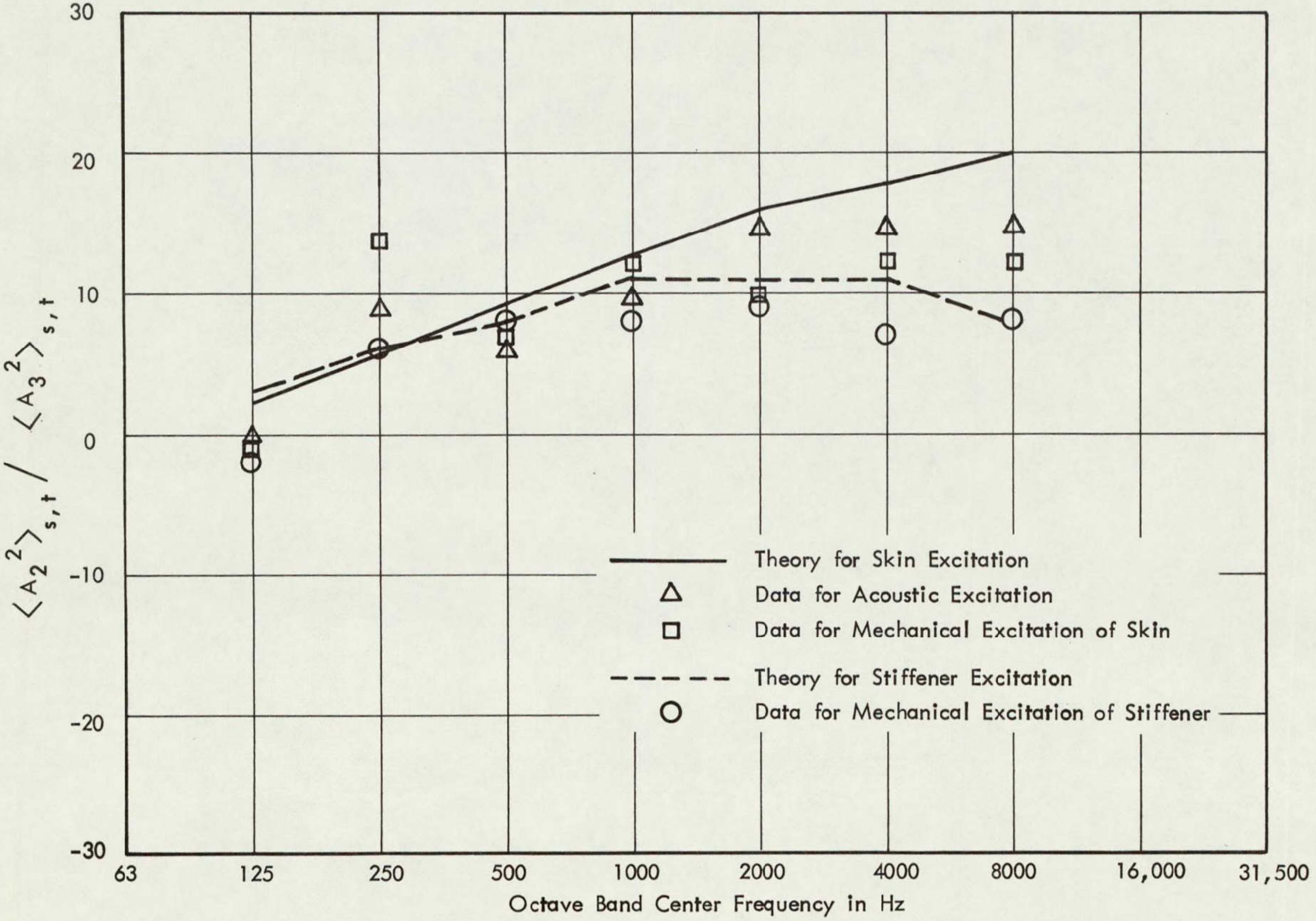

FIGURE 16. RATIO OF SPACE-TIME MEAN SQUARE SKIN ACCELERATION TO SPACE-TIME MEAN SQUARE STIFFENER ACCELERATION

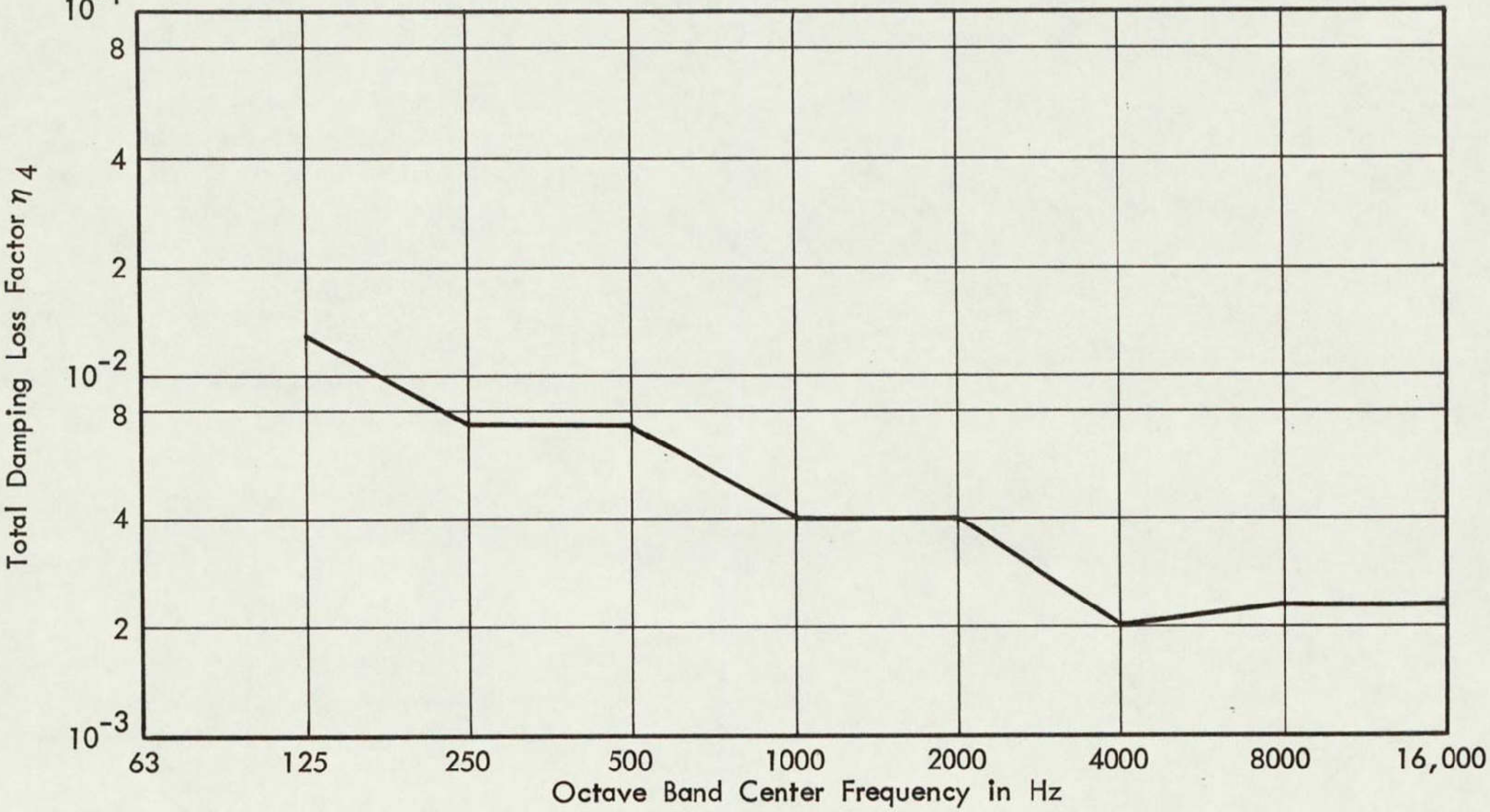

FIGURE 17. MEASURED BOX TOTAL DAMPING LOSS FACTOR

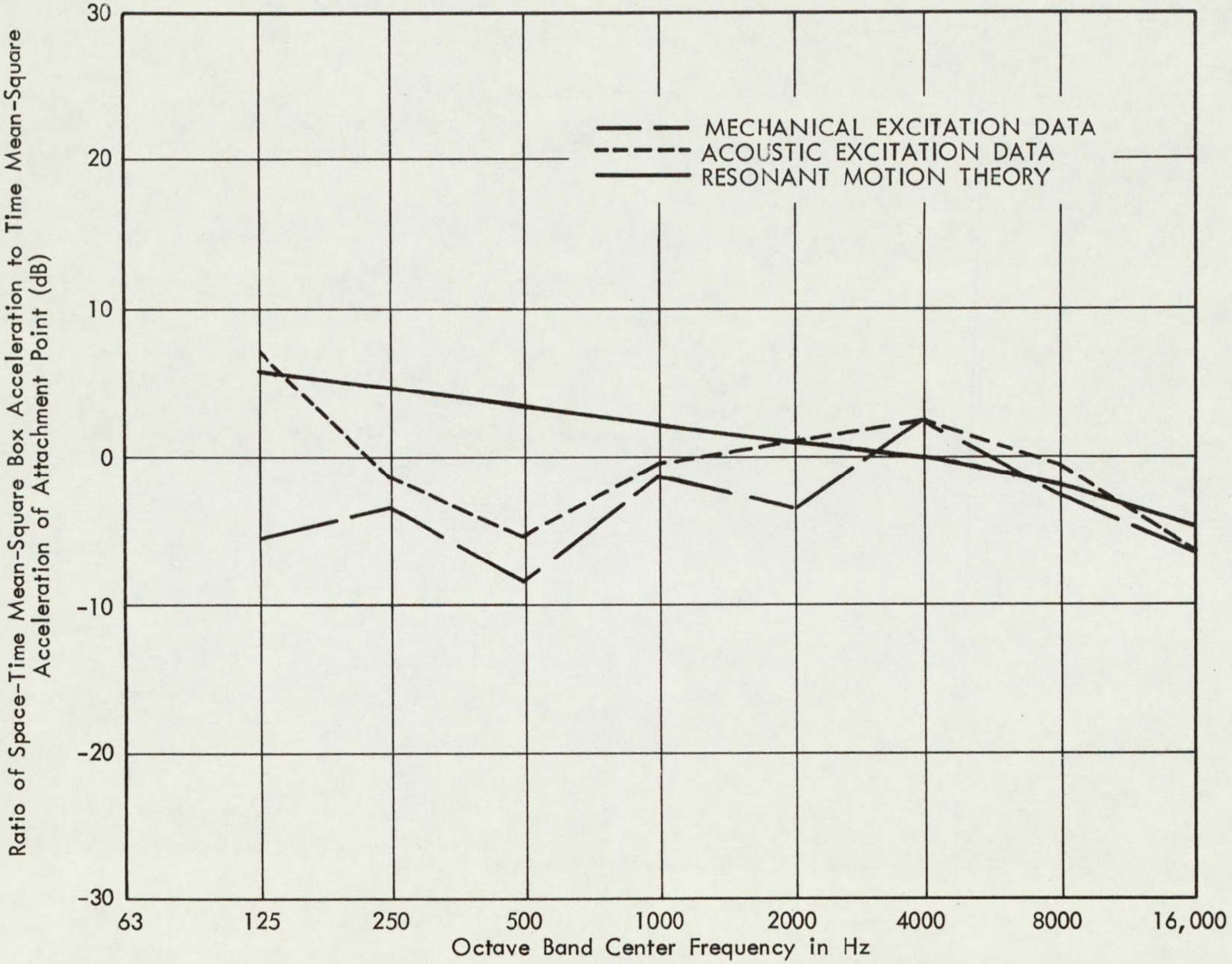

FIGURE 18. ACCELERATION TRANSFER FUNCTION FROM ATTACHMENT POINT TO BOX

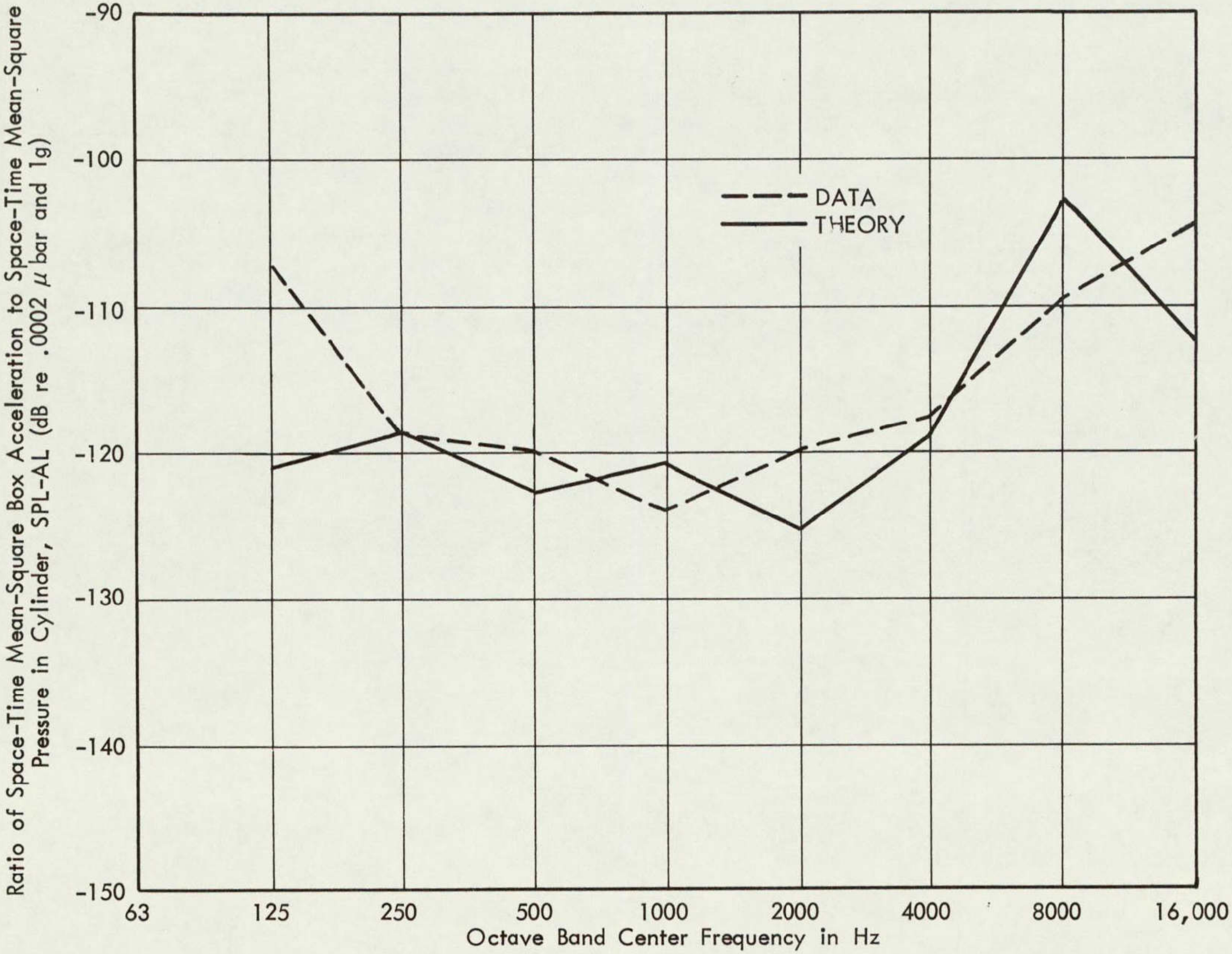

FIGURE 19. ACOUSTIC ACCEPTANCE OF BOX

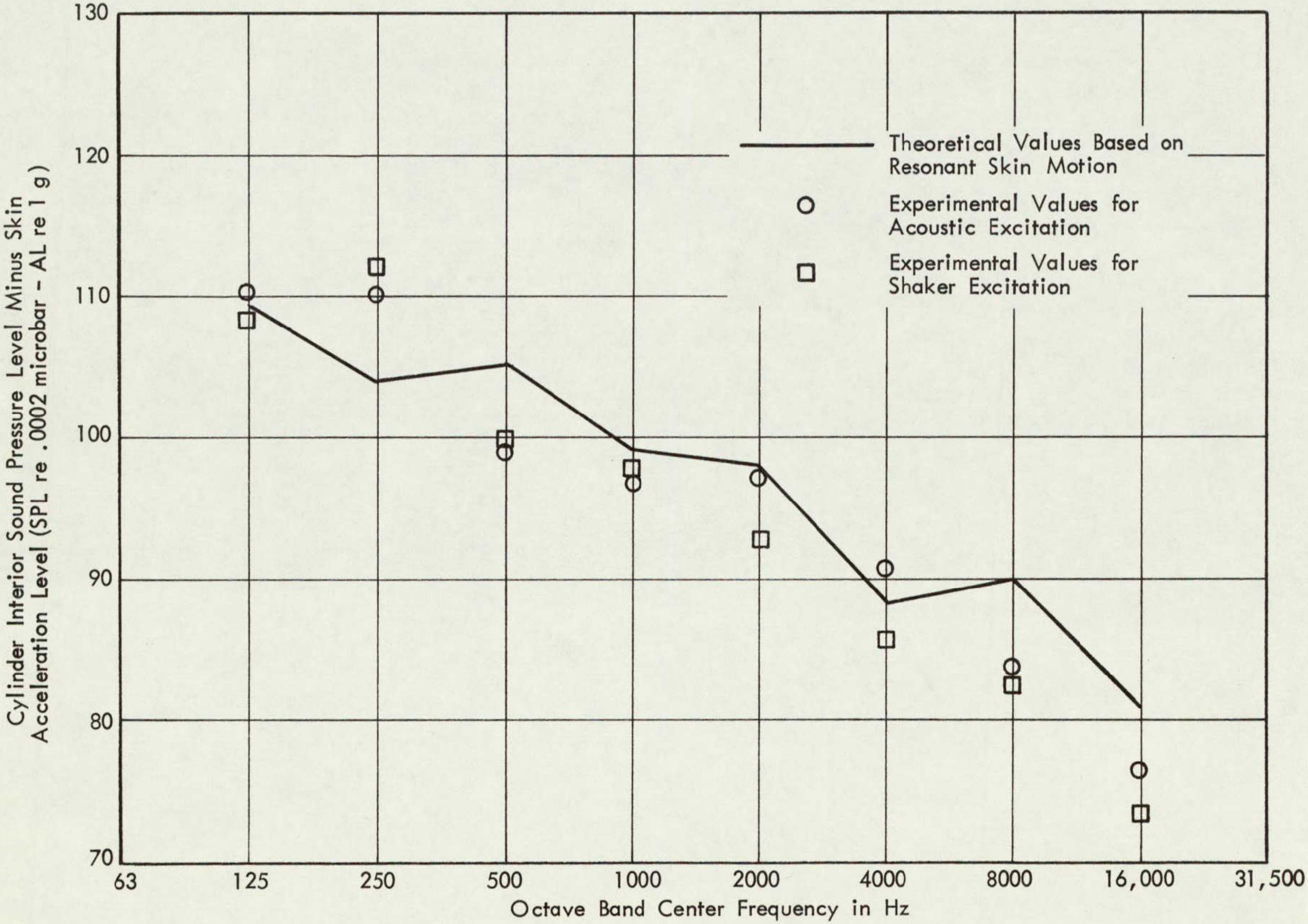

FIGURE 20. RATIO OF CYLINDER INTERIOR SOUND PRESSURE TO SKIN ACCELERATION FOR ACOUSTIC AND SHAKER EXCITATION

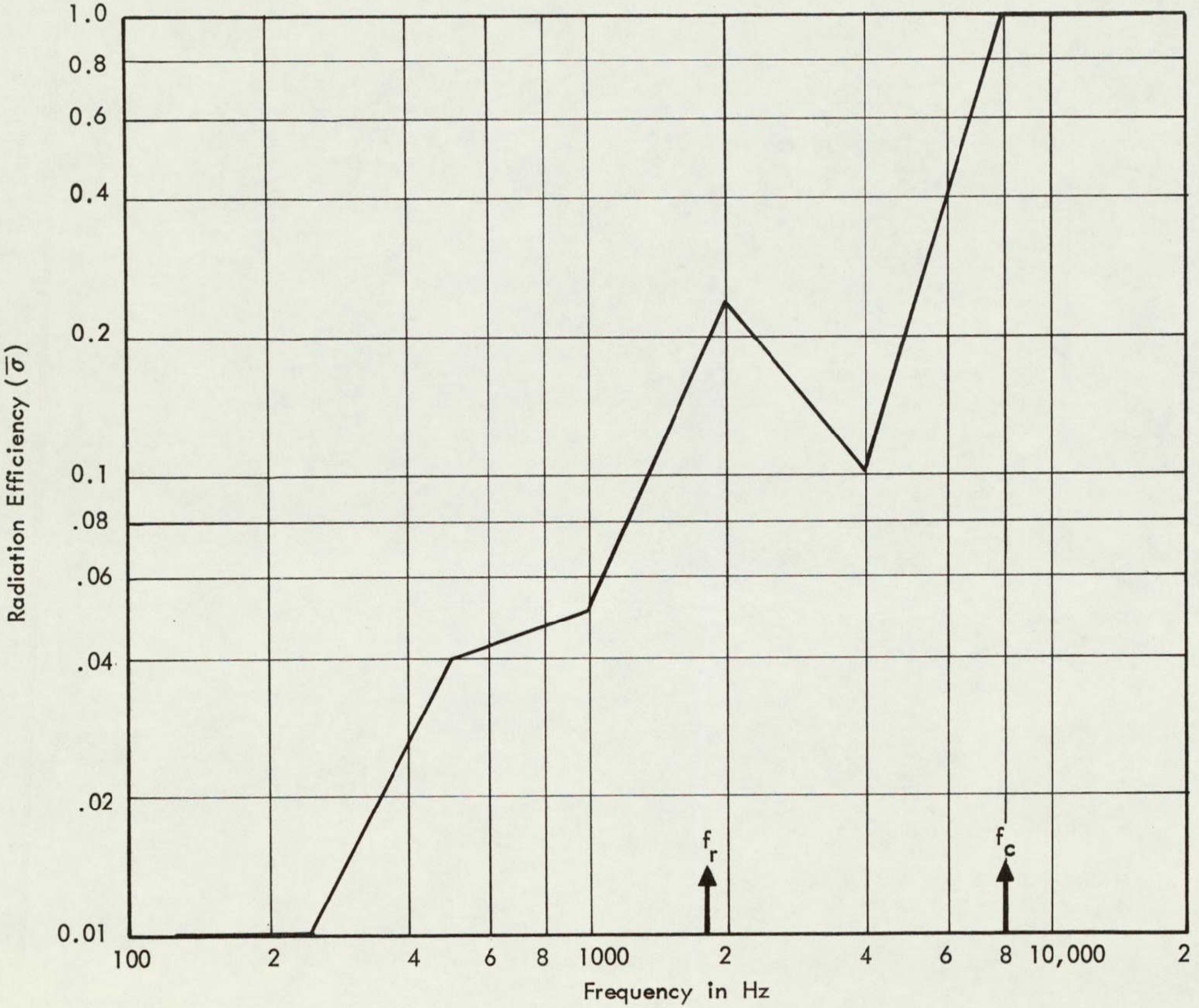

FIGURE 21. AVERAGE MODAL RADIATION EFFICIENCY OF CYLINDER

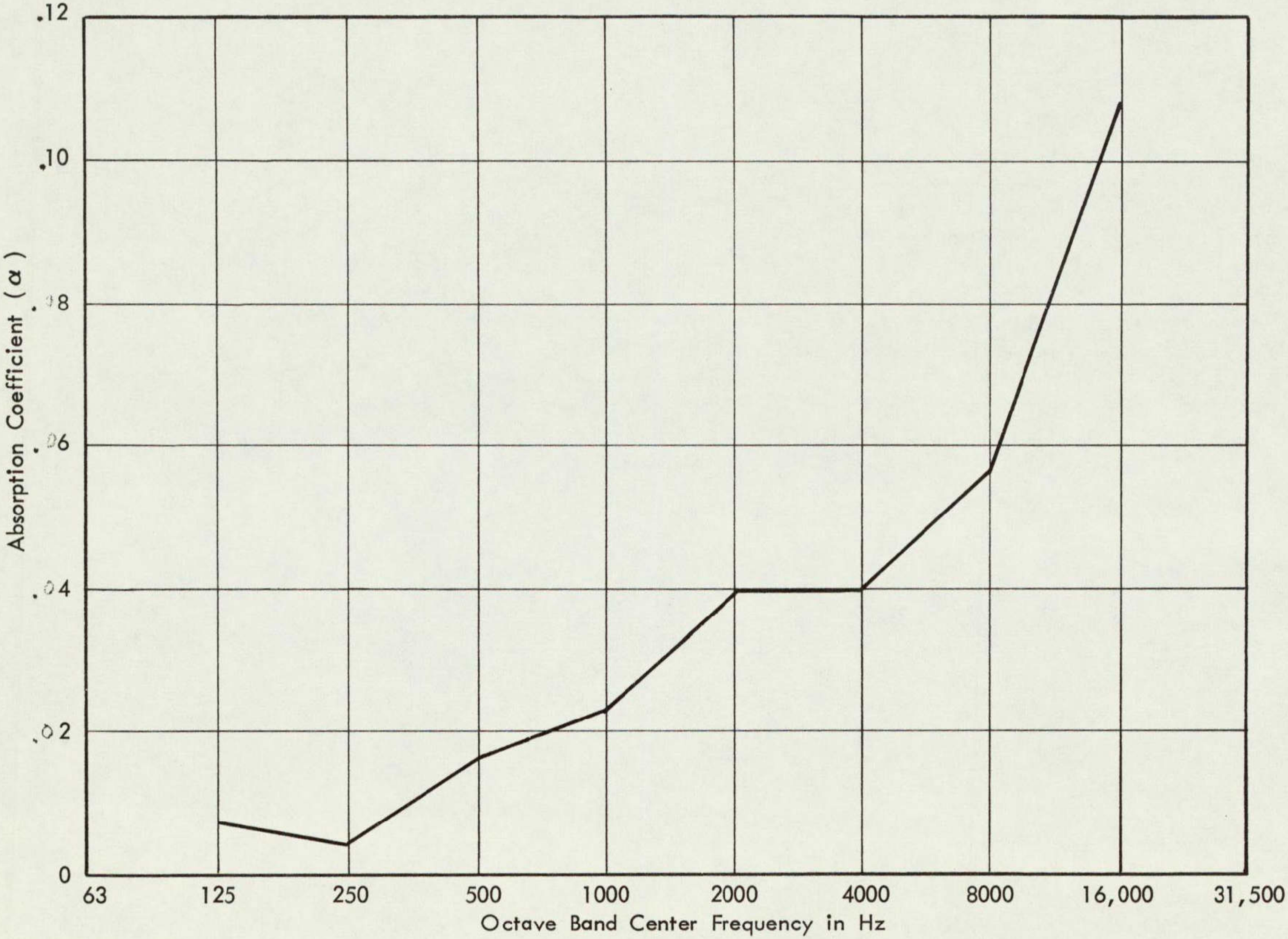

FIGURE 22. MEASURED VALUES OF CYLINDER INTERIOR ACOUSTIC SPACE ABSORPTION COEFFICIENT

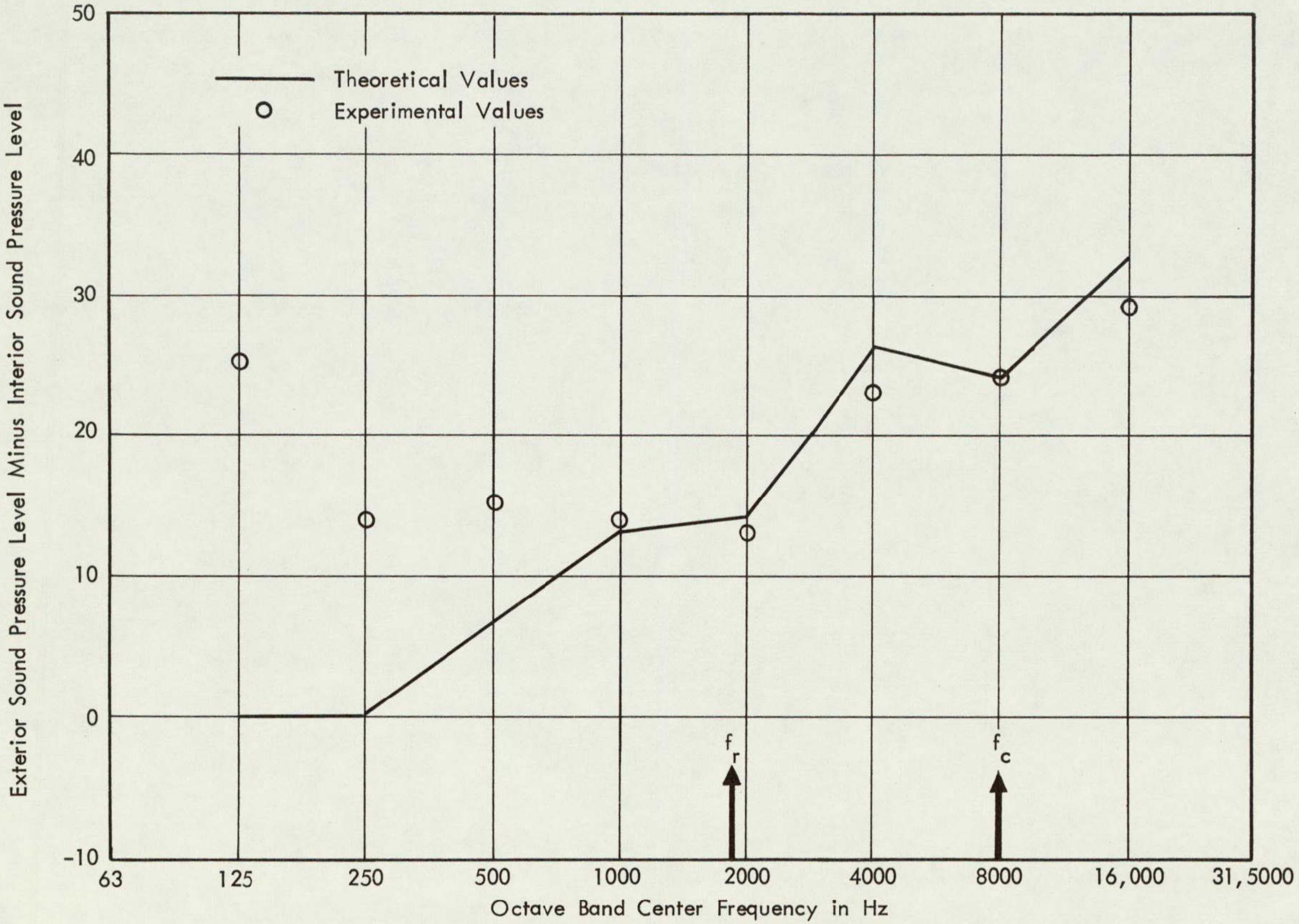

FIGURE 23. THEORETICAL AND EXPERIMENTAL VALUES OF THE CYLINDER NOISE REDUCTION

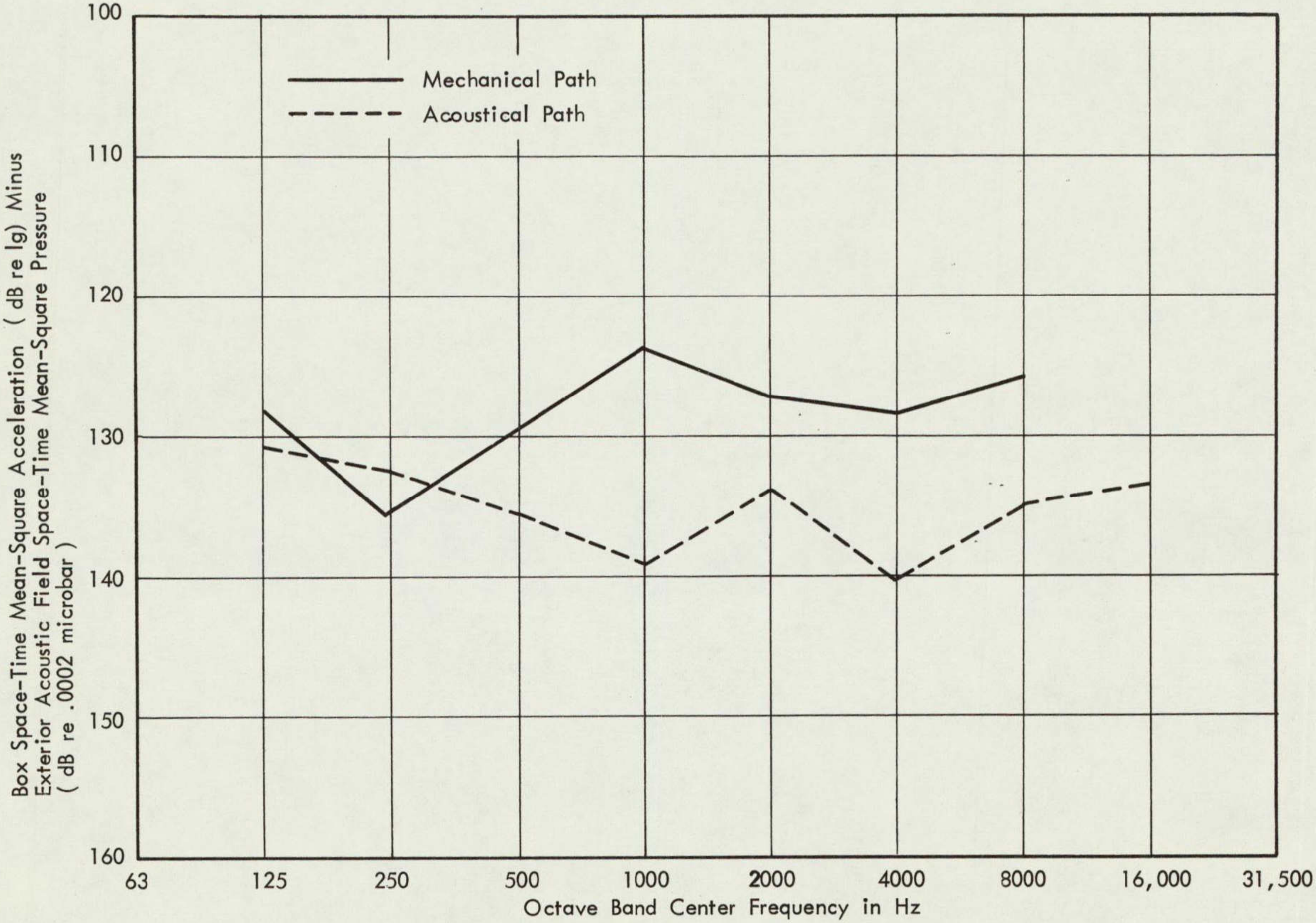

FIGURE 24. COMPARISON OF MEASURED BOX RESPONSES FOR MECHANICAL AND ACOUSTICAL TRANSMISSION PATHS

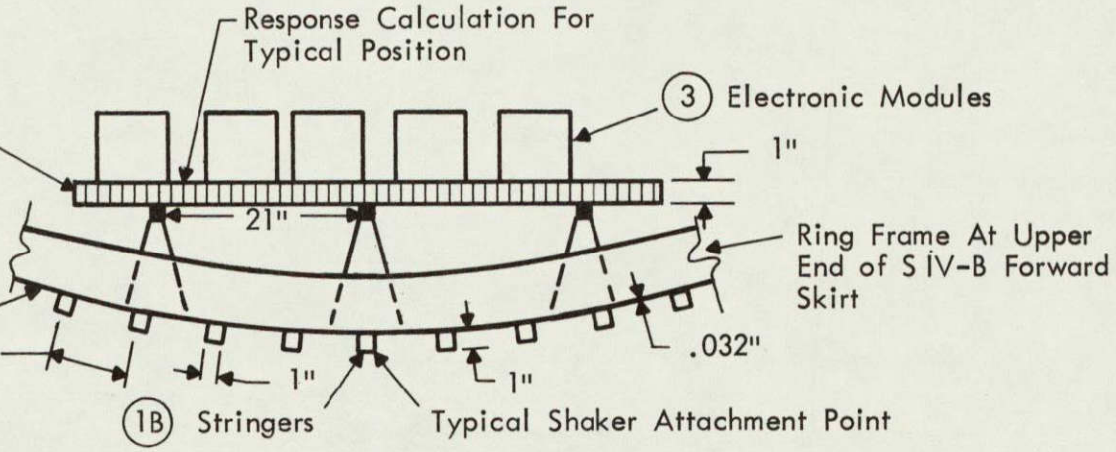

FIGURE 25. TOP VIEW OF PANEL AND MOUNTING CONFIGURATION

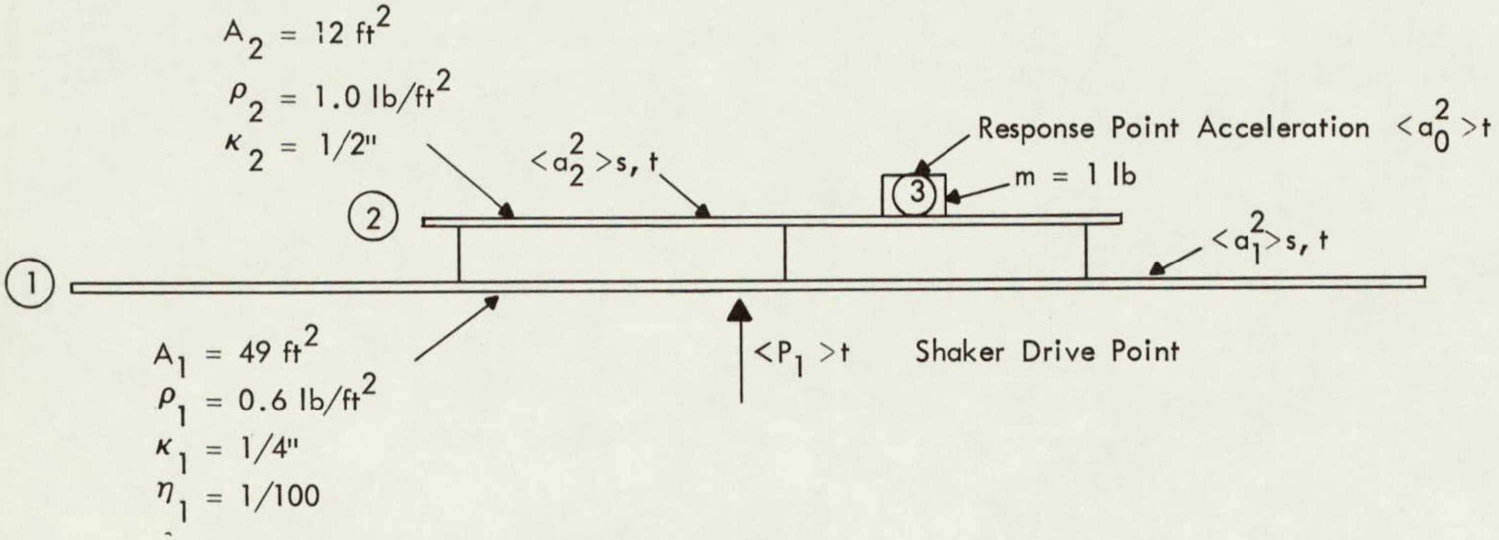

FIGURE 26. IDEALIZED MODEL OF PANEL AND MOUNTING CONFIGURATION

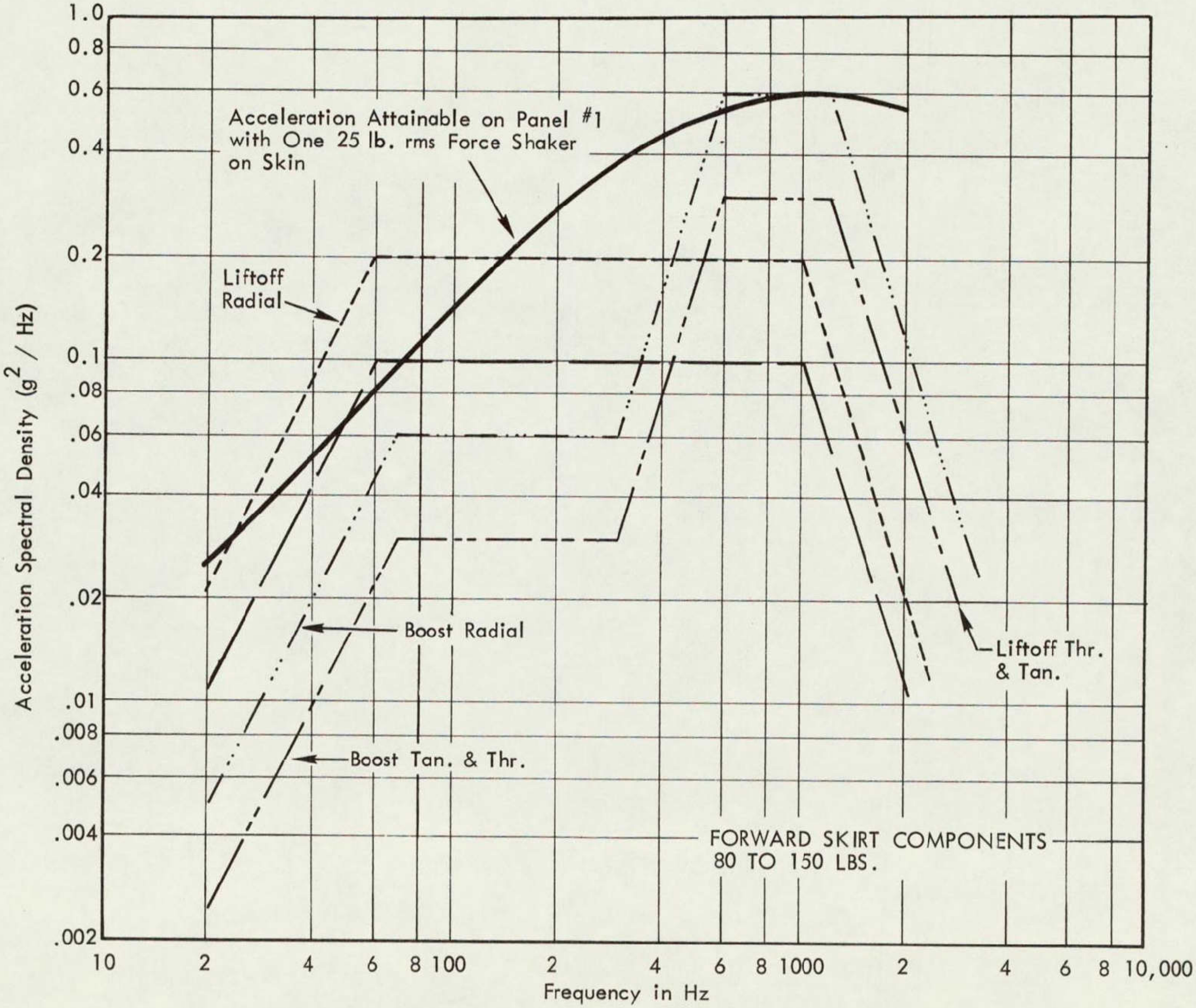

FIGURE 27. COMPARISON OF SMALL SHAKER TEST LEVELS WITH QUALIFICATION VIBRATION TEST SPECIFICATIONS

APPENDIX

STATISTICAL ENERGY ANALYSIS FORMALISM

The theoretical predictions of the cylinder response to acoustical and mechanical excitation are based on the Statistical Energy Analysis technique which has been previously described.[2,3,11,14, and 20] Since this relatively new technique is not widely used, a formal overview of the technique is given here.

Figure A.1 presents a power flow diagram for two coupled linear vibratory acoustical or mechanical systems. In Fig. A.1, $P_i(\Delta f)$ represents the time-average power flow in the frequency band Δf into system i from an external broadband random source, E_i represents the time-average energy of system i, P_{ii} represents the time-average power dissipated in system i, and P_{ij} represents the time-average power transferred from system i to system j. The parameters which describe system i are the dissipation loss factor η_i, and the modal density N_i. The coupling between system i and system j is described by the coupling loss factor η_{ij}. The variables and parameters germane to system j are defined similarly.

The time-average power dissipated in system i is given by

$$P_{ii} = 2\pi f \eta_i E_i \quad , \qquad \text{(A.1)}$$

where f is the center frequency of the band Δf, and the time-average power transferred from system i to system j is given by

$$P_{ij} = 2\pi f \eta_{ij} N_i \left(\frac{E_i}{N_i} - \frac{E_j}{N_j}\right) \quad . \qquad \text{(A.2)}$$

The convention for power flow is such that

$$P_{ij} = -P_{ji} \tag{A.3}$$

and reciprocity demands that the coupling loss factors and modal densities obey

$$N_i\eta_{ij} = N_j\eta_{ji} \tag{A.4}$$

Using Eqs. A.1-A.4 and the diagram of Fig. 1.A, the power balance equations for systems i and j are

$$P_i(\Delta f) = 2\pi\eta_i E_i + 2\pi f\eta_{ij}N_i\left(\frac{E_i}{N_i} - \frac{E_j}{N_j}\right) \quad , \tag{A.5}$$

and

$$P_j(\Delta f) = 2\pi f\eta_j E_j + 2\pi f\eta_{ji}N_j\left(\frac{E_j}{N_j} - \frac{E_i}{N_i}\right) \quad . \tag{A.6}$$

Often only one of the two systems is driven externally, for example system i. In this case, the ratio of the time-average vibratory energies of the two systems is found by solving Eq. A.6 with $P_j(\Delta f) = 0$, which yields

$$\frac{E_j}{E_i} = \frac{N_j}{N_i}\,\frac{\eta_{ji}}{\eta_{ji} + \eta_j} \tag{A.7}$$

Equation A.7, the central result of this appendix is used extensively in the analyses contained in this report. The system energies E_j and E_i are easily related to the space-time mean-square pressure of an acoustic system or the space-time mean-square acceleration of a vibratory mechanical system.

In this investigation of the response of a ring-stringer stiffened cylinder to acoustical and mechanical excitation, it is convenient to divide the vibratory system up into five subsystems: (1) the exterior acoustic field, (2) the cylinder skin, (3) the stiffening rings and stringers, (4) the box mounted to the stiffeners inside the cylinder, and (5) the cylinder interior acoustic field. In the analyses of the system it is assumed that each of these subsystems are lightly coupled so that Eq. A.7 may be applied to each adjacent coupled pair of subsystems.

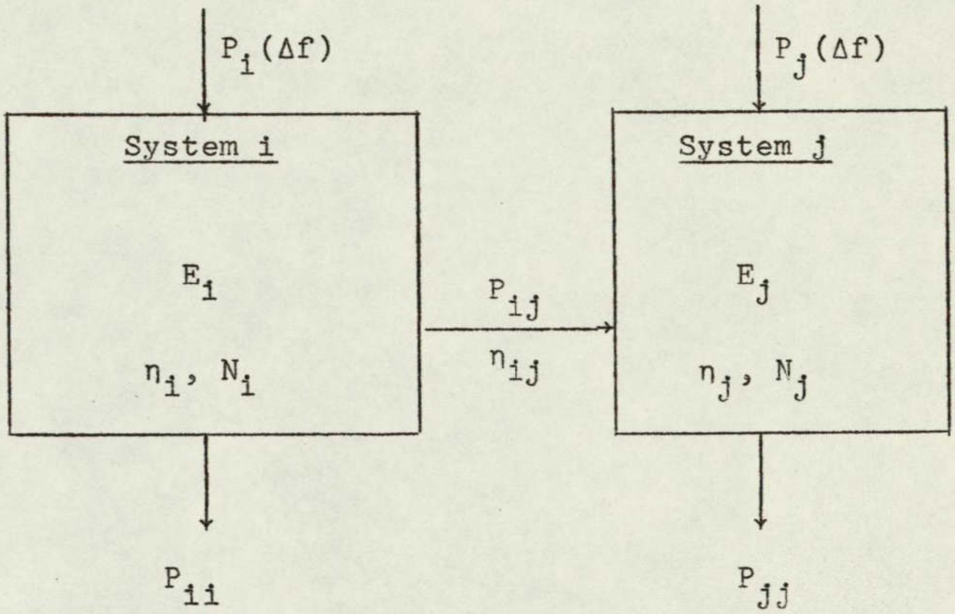

FIGURE A.1 POWER FLOW DIAGRAM FOR STATISTICAL ENERGY ANALYSIS